Article

Photothermal-promoted anion exchange membrane seawater electrolysis on a nickel-molybdenum-based catalyst

Check for updates

Libo Wu [1,2], Wanheng Lu[1], Wei Li Ong[1], Andrew See Weng Wong[3], Yuanming Zhang[1], Tianxi Zhang[1], Kaiyang Zeng [4], Zhifeng Ren [5] ✉ & Ghim Wei Ho [1,2,6] ✉

Exploring active, durable catalysts and utilizing external renewable energy sources offer notable opportunities for advancing seawater electrolysis. Here, a multifunctional NiMo-based catalyst (NiMo-H_2) composed of bimetallic $Ni_{0.91}Mo_{0.09}$ nanoparticles on MoO_2 nanorods is demonstrated for the alkaline seawater hydrogen evolution reaction. The alloying effect and the nanorod-nanoparticle structure endow this catalyst with high structural stability, rapid electron transfer, and a large surface area. The in situ-generated alloyed nanoparticles have notable light absorption and photothermal conversion capabilities, while the vertically grown nanorods suppress diffuse reflection, enabling efficient localized photoheating. Consequently, light irradiation boosts the catalyst's activity and it works stably at a current density of $500\ mA\ cm^{-2}$ in alkaline seawater. We then assemble the NiMo-H_2||NiFe LDH pair in a photothermal anion exchange membrane electrolyzer, and it requires approximately 1.6 V to drive a current of 0.45 A, demonstrating robust durability in overall alkaline seawater electrolysis. This photothermal-promoted seawater electrolysis system shows notable potential for hydrogen production from seawater.

Hydrogen plays a key role in building a low-carbon society because of its wide range of applications in transport, heat, and petroleum/metal refining[1]. Water or seawater electrolysis powered by renewable energy is a zero-carbon-emission conversion pathway for green hydrogen production. The latter is especially attracting widespread research interest because of its inexhaustible resource reserve and its promise in producing hydrogen without exacerbating freshwater shortages[2–5]. However, water/seawater electrolysis is an energetically uphill reaction that requires catalysts able to reduce the overpotential (η) of its two half reactions: the hydrogen evolution reaction (HER) and the oxygen evolution reaction (OER)[6,7]. In particular, seawater electrolysis is typically conducted under alkaline conditions, and an additional water-dissociation step with sluggish kinetics is involved in the alkaline HER[8–10]. Therefore, highly active and durable HER catalysts, especially those capable of sustaining large current densities ($\geq 500\ mA\ cm^{-2}$), are required to promote seawater dissociation and reduce overall energy consumption. At the same time, seawater electrolysis faces challenges such as catalyst structural collapse, low conductivity, the chlorine evolution reaction (ClER), and precipitate coverage that need to be overcome through rational catalyst design. Another important issue is that practical overall water electrolysis is normally carried out in a sealed electrolyzer, which includes the membrane electrode assembly

[1]Department of Electrical and Computer Engineering, National University of Singapore, Singapore, Singapore. [2]Centre for Hydrogen Innovations, National University of Singapore, Singapore, Singapore. [3]Facility for Analysis Characterization Testing and Simulation (FACTS), Nanyang Technological University, Singapore, Singapore. [4]Department of Mechanical Engineering, National University of Singapore, Singapore, Singapore. [5]Department of Physics and Texas Center for Superconductivity at the University of Houston (TcSUH), University of Houston, Houston, TX, USA. [6]Department of Materials Science and Engineering, National University of Singapore, Singapore, Singapore. ✉e-mail: zren@uh.edu; elehgw@nus.edu.sg

(MEA), electrolyte flow control, and production gas separation, and this has been inadequately studied for seawater electrolysis. Thus, focusing on catalysts alone may not provide a comprehensive assessment of the hydrogen production capabilities of the entire system[11].

As early as 1980, Bennett investigated the use of oxygen-selective electrodes to produce hydrogen through direct seawater electrolysis[4]. More recently, great advances have been made in this field since Dionigi et al. analyzed the scientific basis for alkaline seawater electrolysis and investigated using NiFe LDH catalyst for this in 2016[10,12–16]. However, most of these advances have focused on the design and optimization of catalysts to address their fundamental scientific challenges in seawater electrolysis. There have been fewer innovations in external energy utilization or advanced seawater electrolysis electrolyzer design (Supplementary Table S1), both of which may offer promising solutions for hydrogen production from seawater[5,16–20]. For example, hot coastal areas have abundant clean and free solar energy resources (Supplementary Fig. S1), providing photothermal energy that can accelerate the movement of reactants and reduce the activation energy barrier, thereby promoting catalytic reactions. In contrast to traditional methods that heat up the entire system, increasing energy consumption and electrolyzer complexity, photothermal heating is a direct and efficient method and can be localized to the catalyst. Various photothermal materials have been explored and utilized for highly effective light-to-heat conversion in diverse research areas[21,22]. However, there are few studies on photothermal materials in the field of seawater electrolysis, especially on the photothermal electrolyzer system[8,23,24]. If photothermal energy resources can be effectively harvested and utilized through the rational design of catalysts and electrolyzers, it will facilitate the sustainable development of seawater electrolysis. To achieve this goal, two major challenges must be overcome: the efficient absorption of solar energy and its conversion into heat, and the thermal management of heat concentrated in the catalytic reaction regions. First, it is necessary to explore catalysts that have both good light absorption and photothermal conversion capabilities to maintain the spatial consistency between photoheating and catalytic reactions, maximizing the photothermal effect on the catalytic reaction. These catalysts should also exhibit high intrinsic catalytic activity and resistance to severe degradation during catalytic reactions in seawater. Second, when designing a photothermal electrolyzer, thermal diffusion must be managed to avoid rapid heat loss[25]. The rational design of an effective photothermal electrolyzer is of great significance in advancing photothermal-promoted seawater electrolysis to the level of potential applications, which is highly desired but remains a challenge.

Here we synthesize a hierarchical NiMo-H$_2$ catalyst composed of bimetallic Ni$_{0.91}$Mo$_{0.09}$ nanoparticles on a MoO$_2$ nanorod matrix for photothermal-promoted alkaline seawater HER (Fig. 1a). The size of these nanoparticles, which are generated in situ and tightly bound to the nanorods, is maintained between 20 and 40 nanometers, ensuring their full exposure to the electrolyte and preventing aggregation during the catalytic reaction. Theoretical calculations reveal that the electronic tuning between the Ni and Mo atoms endows the Mo sites with high water adsorption and dissociation capabilities, thereby accelerating the sluggish catalytic kinetics. High-temperature hydrogen reduction during the synthesis process endows the NiMo-H$_2$ catalyst with high conductivity and good thermodynamic stability, enabling it to work well in seawater without severe structural collapse. More importantly, the catalytically active Ni$_{0.91}$Mo$_{0.09}$ nanoparticles have good light harvesting and photothermal conversion capabilities and can achieve in situ photoheating under light irradiation. When placed in a photothermal electrolyzer with effective thermal diffusion management, the mass transfer and catalytic kinetics can be accelerated while the activation energy barrier is reduced by increasing the local reaction temperature through photothermal effects. As a result, the catalytic performance of this multifunctional NiMo-H$_2$ catalyst is

effectively promoted, making it among the most efficient alkaline seawater HER catalysts[26–28]. At the same time, its hierarchical nanorod-nanoparticle structure enlarges the surface area and reduces the impact of precipitate coverage, and the hydrophilic surface can accelerate gas release and provide good catalytic durability at large current densities. As a result, the NiMo-H$_2$ catalyst can sustain continuous testing for 540 h at a constant current density of 500 mA cm^{-2} in 6 M KOH seawater electrolyte. A photothermal anion exchange membrane (AEM) electrolyzer is then designed for photothermal-promoted overall seawater electrolysis (Fig. 1b). The NiMo-H$_2$||NiFe LDH pair requires low voltages of approximately 1.40, 1.51, and 1.80 V to reach absolute currents of -0.0225, 0.225, and 1.8 A (area: 2.25 cm^2), respectively, in 6 M KOH seawater under one sun irradiation and can work at a constant current of 0.45 A for 192 h. This pair also shows high Faradaic efficiency without forming hydrochloride during alkaline seawater electrolysis. This work demonstrates a strategy to design and prepare promising catalysts and electrolyzers for efficient photothermal-promoted seawater electrolysis and offers prospects for hydrogen production from seawater.

Results and discussion
Catalyst synthesis and characterization
As illustrated in Supplementary Fig. S2, self-supported NiMo-H$_2$ catalyst was grown in situ on conductive substrates (nickel or copper foam, Supplementary Fig. S3) through a two-step water bath reaction and hydrogen reduction procedure (see experimental details in the Methods). Corresponding photographs demonstrate that the nickel foam (NF) substrate, NiMoO$_4$·xH$_2$O precursor, and NiMo-H$_2$ catalyst are grey, brown, and black, respectively, in color (Supplementary Fig. S2). X-ray diffraction (XRD) and Raman measurements were carried out to analyze the composition of these as-synthesized samples. The XRD pattern in Supplementary Fig. S4a indicates the successful synthesis of the NiMoO$_4$·xH$_2$O phase through the first-step water bath reaction. After hydrogen reduction in the second step, the NiMoO$_4$·xH$_2$O precursor transformed into Ni$_{0.91}$Mo$_{0.09}$ and MoO$_2$ phases (Supplementary Fig. S4c), thereby constituting the NiMo-H$_2$ catalyst. The phase transition due to hydrogen reduction can be further confirmed by the corresponding Raman results. As shown in Supplementary Fig. S4d, the intensity of the Raman peaks at 818, 889, and 938 cm^{-1} in the spectrum for the NiMo-H$_2$ catalyst, attributed to the Mo−O vibration, is much weaker than that for the NiMoO$_4$·xH$_2$O precursor (Supplementary Fig. S4b)[27,29]. Meanwhile, the Raman peak at ~371 cm^{-1}, which should be ascribed to Ni−O−Mo vibration, is sharply reduced and no single peak for Ni−O is observed for the NiMo-H$_2$ catalyst. The NiMo-Air catalyst was synthesized by annealing the NiMoO$_4$·xH$_2$O precursor in air. Its color is similar to that of the precursor (Supplementary Fig. S2) and it is composed of the NiMoO$_4$ phase (Supplementary Fig. S4e, f). Apparently, the different compositions of NiMo-H$_2$ and NiMo-Air result from the fact that annealing in air mainly removes water, while reduction in hydrogen not only removes water but also reduces Ni and Mo to their lower valence states, forming new phases.

Following compositional characterization, the structure of each sample was analyzed using scanning electron microscopy (SEM) and transmission electron microscopy (TEM). As shown in Supplementary Fig. S5, after the water bath reaction, the conductive substrate was uniformly covered with the NiMoO$_4$·xH$_2$O precursor, which has a one-dimensional nanorod structure with a diameter less than 300 nm. The smooth surface of these nanorods became rough in NiMo-Air due to water loss during high-temperature annealing in air (Supplementary Fig. S6). On the other hand, upon hydrogen reduction, the structure of these nanorods underwent different changes in NiMo-H$_2$: the macroscopic nanorod structure was preserved (Supplementary Fig. S7a−c), but nanoparticles with a size distribution between 20 and 40 nm were newly formed on the surfaces of these nanorods (Fig. 1c, d,
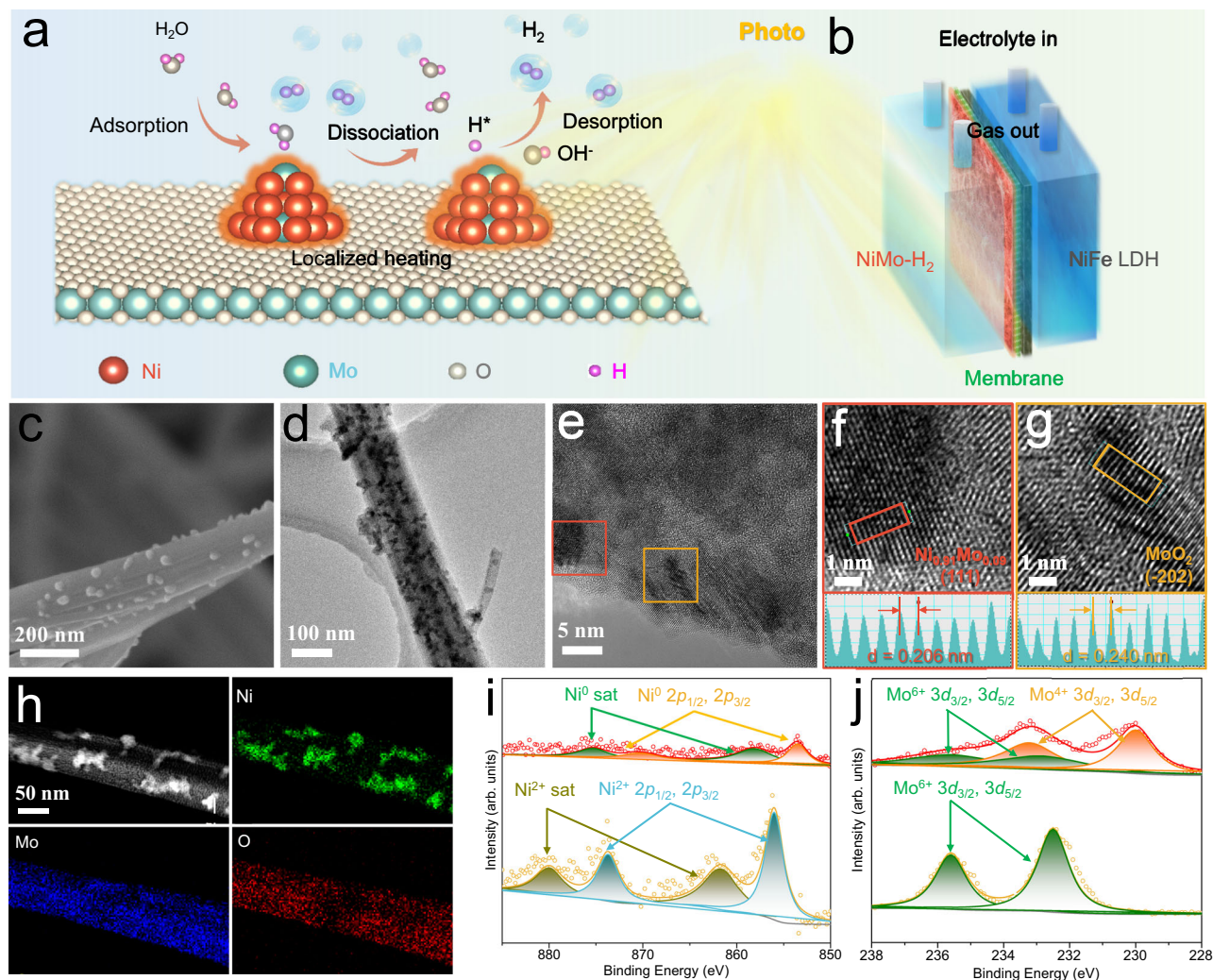
Fig. 1 | Working scheme and structural and compositional characterizations of NiMo-H₂ catalyst. Schematic illustrations of (**a**) the working mechanism for photothermal-promoted alkaline seawater HER over the NiMo-H₂ catalyst and (**b**) the photothermal-promoted AEM seawater electrolyzer. (**c**) SEM, (**d**) TEM, and (**e–g**) HRTEM images of NiMo-H₂. The red and orange boxes indicate the magnified regions. d represents the interplanar spacing. (**h**) High-angle annular dark field image of NiMo-H₂ and the corresponding EDS mapping for elemental Ni, Mo, and O. High-resolution XPS spectra of (**i**) Ni and (**j**) Mo for NiMoO₄·xH₂O (bottom) and NiMo-H₂ (top). Source data are provided as a Source Data file.

Supplementary Fig. S7d–f, and Supplementary Fig. S8a–c). To identify the composition of these nanoparticles and nanorods in detail, high-resolution TEM (HRTEM), selected area electron diffraction (SAED), and energy-dispersive X-ray spectroscopy (EDS) characterizations were performed. As shown in the HRTEM images in Fig. 1e–g and Supplementary Fig. S8d–e, the interplanar spacings of the lattice fringes in the nanoparticles measured 0.206 nm, which corresponds to the (111) plane of the $Ni_{0.91}Mo_{0.09}$ alloy, whereas lattice stripes with an interplanar spacing of 0.240 nm were detected in the rods, which corresponds to the (202) plane of MoO_2. The coexistence of $Ni_{0.91}Mo_{0.09}$ and MoO_2 phases in NiMo-H₂ catalyst was also confirmed by the SAED and TEM EDS mapping results. As illustrated in Supplementary Fig. S8c, the characteristic (111) and (200) facets of $Ni_{0.91}Mo_{0.09}$ and (031) facet of MoO_2 can be identified in the SAED pattern of the NiMo-H₂ sample. TEM EDS mapping images in Fig. 1h show that elemental Ni can only be found in the nanoparticles, while elemental Mo and O were observed throughout the entire nanorod. Detailed TEM EDS spectral analysis on single nanoparticle confirms the co-existence of Ni and Mo and the Ni/Mo ratio of 9/1 (Supplementary Fig. S8h, i). Previous studies proposed that when the Ni–Mo–O precursor is reduced in a reductive gas flow, there may be a preferential

reaction at the Ni sites, and that Mo reduction proceeds by hydrogen spillover from these Ni sites[30,31]. Based on the above compositional and structural analyses, we speculate that the hierarchical nanorod-nanoparticle-structured NiMo-H₂ catalyst forms as follows: during hydrogen reduction, Ni is first reduced and aggregated on the surface, and is then alloyed with hydrogen-reduced Mo to form Ni-rich bimetallic Ni-Mo alloy nanoparticles[30,32]. Simultaneously, other parts of the nanorod transform into MoO_2 due to the movement of Ni and the reduction of Mo. Furthermore, the loss of water molecules and elemental oxygen during the hydrogen reduction process creates rich atomic defects and leads to disordered atom packing, forming abundant amorphous regions in the nanorods as revealed by the HRTEM images in Supplementary Fig. S8f, g. The surface area of these samples was then analyzed using the Brunauer–Emmett–Teller (BET) method. As shown in Supplementary Fig. S9, the BET surface area of NiMo-H₂ catalyst (48.3 m² g⁻¹) is around 3.5 times that of the MoO₄·xH₂O precursor (13.7 m² g⁻¹), allowing for exposing more active sites for catalytic reaction. Meanwhile, such a well-designed hierarchical nanorod-nanoparticle structure endows the catalyst with ample surface area and roughness, enhancing light absorption by suppressing diffuse reflection. In addition, the bimetallic Ni-Mo alloy nanoparticles

maximize the use of surface atoms to participate in catalytic reactions and shorten charge diffusion distance, thus boosting the catalytic performance.

Since catalytic reactions occur on the surface of the catalyst and are closely related to the coordination environment of its constituent elements, the surface chemical valence state of these catalysts was determined using X-ray photoelectron spectroscopy (XPS). In the high-resolution Ni XPS spectrum for the $NiMoO_4 \cdot xH_2O$ precursor (Fig. 1i), two peaks assigned to Ni^{2+} $2p_{3/2}$ and Ni^{2+} $2p_{1/2}$ are observed at 856.2 and 873.8 eV, respectively, along with a pair of satellite peaks[33]. After hydrogen reduction, the peaks attributed to Ni^{2+} $2p$ disappear, and two new peaks located at 853.6 and 870.2 eV, as well as two accompanying satellite peaks, emerge for $NiMo-H_2$. These newly formed peaks are assigned to the Ni^0 $2p$ species in the bimetallic $Ni_{0.91}Mo_{0.09}$ phase[26,30]. Regarding the Mo XPS spectrum for $NiMoO_4 \cdot xH_2O$ (Fig. 1j), the peaks at 232.4 and 235.6 eV are assigned to Mo^{6+} $3d_{5/2}$ and Mo^{6+} $3d_{3/2}$, respectively[34]. The intensity of these peaks is greatly reduced in $NiMo-H_2$, and two new XPS peaks corresponding to Mo^{4+} $3d_{5/2}/3d_{3/2}$ can be observed at 230 and 233.2 eV, respectively, confirming that hydrogen reduction lowers the valence states of Mo from 6+ to 4+[26,35]. Similarly, the intensity of the O $1s$ peak attributed to the Mo–O bond in the $NiMoO_4 \cdot xH_2O$ precursor is also reduced in $NiMo-H_2$ after hydrogen reduction (Supplementary Fig. S10). The above valence state analysis indicates that Ni and Mo mainly exist as metallic Ni and Mo^{4+}, respectively, in $NiMo-H_2$, consistent with the XRD results. X-ray absorption spectroscopy (XAS) was performed to analyze the Ni element in the $NiMo-H_2$, with Ni foil and NiO as the reference samples. As shown in Supplementary Fig. S11a, Ni K-edge X-ray absorption near edge structure (XANES) spectra in $NiMo-H_2$ present a similar absorption edge to that of the Ni foil reference, but greatly differ from that of NiO, indicating the metallic nature of Ni in the $NiMo-H_2$[36]. The chemical environment around Ni was determined to be slightly different in $NiMo-H_2$ compared to Ni foil reflected by the extended X-ray absorption fine structure (EXAFS) spectra in the k-space and the corresponding Fourier transform in the R-space (Supplementary Fig. S11b–d)[37,38]. In addition, fitting data in Supplementary Table S2 shows the $NiMo-H_2$ model has an average Ni-Ni coordination number (CN) of 6.4 and an average Ni-Mo CN of 1.4, which is distinctive from the Ni-Ni CN (12) in metallic Ni foil reference. The results from EXAFS wavelet transform (Supplementary Fig. S11e–g) exhibit that the intensity maximum at ~7.0 Å^{-1} in k space that corresponds to Ni–Ni and Ni–Mo bonds in $NiMo-H_2$.
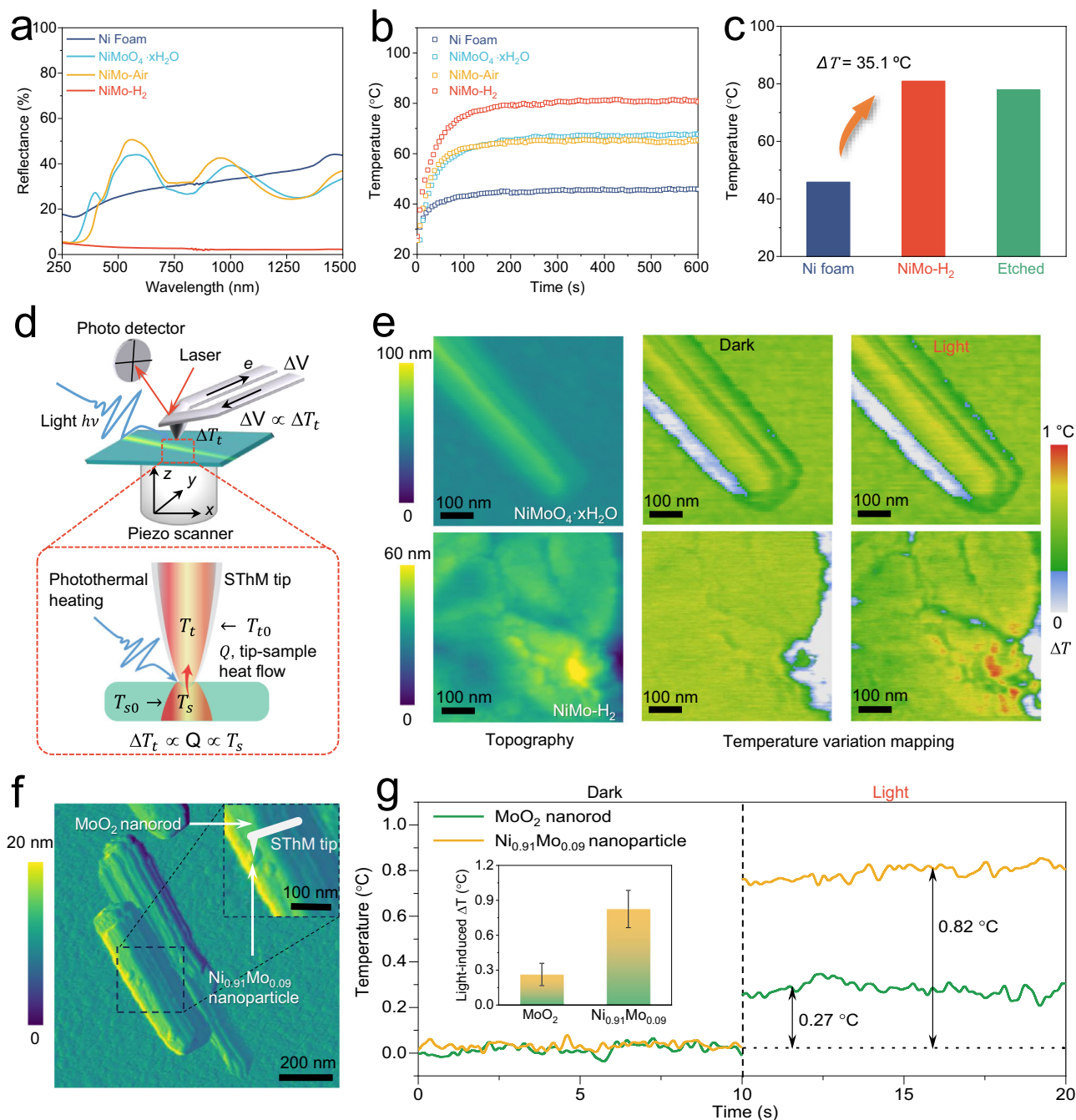
Photo-to-thermal performance analysis

To investigate the photothermal properties of these samples, their light reflectance abilities were first determined using ultraviolet–visible–near-infrared (UV–vis–NIR) diffuse reflectance spectroscopy. The reflectance curves in Supplementary Fig. S12 show that the $NiMoO_4 \cdot xH_2O$, NiMo-Air, and $NiMo-H_2$ samples all exhibit lower reflectivity in their self-supported state (solid lines) compared to their powder state (dashed lines). This is because the three-dimensional hollow substrate in each of these self-supported samples allows light to be absorbed by the multilayer catalyst on its surface, thus reducing reflectivity. On the other hand, although these three samples all exhibit a similar nanorod structure at the macroscopic scale, the reflectance of $NiMo-H_2$ is considerably lower than that of the other two, which indicates that hydrogen reduction has a high impact on reducing the reflectivity. Specifically, the self-supported $NiMo-H_2$ exhibits a low reflectance of less than 3% over the wavelength range from 250 to 1500 nm (Fig. 2a), showing its great potential for sunlight utilization. Considering that $NiMo-H_2$ comprises $Ni_{0.91}Mo_{0.09}$ nanoparticles and MoO_2 nanorods, we synthesized powdered Ni-Mo alloy nanoparticles (Supplementary Fig. S13) and MoO_2 nanorods (Supplementary Fig. S14) to determine which of the catalyst's components exhibits more effective light absorption. As shown in Supplementary Fig. S15, the reflectivity of the Ni-Mo alloy nanoparticles is lower

than that of the MoO_2 nanorods at wavelengths greater than 516 nm, indicating the former's more efficient absorption of light over the vis–NIR range.

The temperature change in these samples under light irradiation was subsequently measured using a thermal imaging camera. As illustrated in Fig. 2b and Supplementary Fig. S16, the temperature of the self-supported $NiMo-H_2$ catalyst rapidly reached 80.6 ± 0.2 °C after being exposed to simulated one sun irradiation (100 mW cm^{-2}) for 300 s and then remained relatively stable. This temperature is 13.9 and 16.5 °C higher than that for the $NiMoO_4 \cdot xH_2O$ and NiMo-Air catalysts, respectively, after corresponding exposure to irradiation. In contrast, the blank NF substrate only reached a temperature of 45.8 ± 0.1 °C after 600 s of light irradiation (Fig. 2c), exhibiting the lowest photothermal conversion capability among the studied samples. These findings demonstrate that the $NiMo-H_2$ catalyst grown on the substrate surface is the key component for efficient photothermal conversion and temperature rise. Additionally, all self-supported catalysts reached higher temperatures more rapidly than their powdered counterparts (Supplementary Fig. S17), indicating their more efficient light utilization, which is consistent with their lower reflectance in the UV–vis–NIR measurements. The photothermal conversion efficiency of each powdered sample was calculated by analyzing the temperature evolution curves of its solution with and without light irradiation (Supplementary Fig. S18). Among these samples, $NiMo-H_2$ exhibits the highest photothermal conversion efficiency of 42%, which is more than twice that of the $NiMoO_4 \cdot xH_2O$ precursor (19.5%).

The origin of the enhanced photothermal heating capability of this designed $NiMo-H_2$ catalyst was then explored by measuring the light-induced temperature variations at specific localized areas of the sample using scanning photo-thermal microcopy (SPThM). The working mechanism of the SPThM system, which is based on scanning thermal microscopy (SThM) equipped with a light source, is illustrated in Fig. 2d: when the light source is activated, the temperature of the localized illuminated area of the sample will rise due to the photothermal effect, which will in turn cause heat to flow from the heated sample to the SThM tip, resulting in proportional variations in the tip temperature. The tip temperature variations, and thus the light-induced changes in the sample temperature, can be measured by monitoring the voltage across two bridges of the SThM tip. The nanoscale temperature mappings in Fig. 2e so-obtained demonstrate that there is a considerable temperature increase in the $NiMo-H_2$ sample when illuminated with vis–NIR light irradiation in comparison to the dark conditions. Conversely, the light-induced temperature rise in $NiMoO_4 \cdot xH_2O$ is negligible. This observation aligns with the findings in Fig. 2b, which shows that $NiMo-H_2$ demonstrates a higher photo-to-heat conversion efficiency. Furthermore, two characteristics of the SThM system, namely the tiny temperature sensor and the precise control over the tip position, enable us to localize the SThM tip at a $Ni_{0.91}Mo_{0.09}$ or MoO_2 region within the $NiMo-H_2$ catalyst (Fig. 2f) to determine which component exhibits greater efficacy for photothermal conversion[39]. The temperature profile data in Fig. 2g indicate that the light-induced temperature increase in the $Ni_{0.91}Mo_{0.09}$ nanoparticles (0.82 °C) is approximately three times as high as that for the MoO_2 nanorods (0.27 °C) under the same light irradiation conditions, suggesting more efficient photothermal heating. In fact, if these $Ni_{0.91}Mo_{0.09}$ nanoparticles were partially removed using acid etching, the temperature increase in the etched $NiMo-H_2$ sample under one sun irradiation would be inferior to that in the fresh sample (Fig. 2c and Supplementary Fig. S19). These results, together with the UV–vis–NIR measurements in Supplementary Fig. S15, confirm that, as compared to the MoO_2 nanorods, the $Ni_{0.91}Mo_{0.09}$ alloy nanoparticles with lower reflectivity over the vis–NIR range can utilize light more efficiently and are more effective for photothermal conversion within $NiMo-H_2$. Additionally, the rationally designed nanorod-nanoparticle structure

Fig. 2 | Photothermal performance analysis of catalysts. a UV–vis−NIR reflectance spectra and (**b**) temperature evolution curves under simulated one sun irradiation for the Ni foam substrate and self-supported NiMoO$_4$·xH$_2$O, NiMo-Air, and NiMo-H$_2$ samples. **c** Temperatures of Ni foam and of fresh and etched NiMo-H$_2$ samples after 600 s of simulated one sun irradiation. **d** Schematic illustration of the SPThM. **e** Topography and temperature variation mappings under dark and light conditions for NiMoO$_4$·xH$_2$O and NiMo-H$_2$ samples. **f** AFM image of NiMo-H$_2$ showing that the SthM tip can be located at a Ni$_{0.91}$Mo$_{0.09}$ or MoO$_2$ region inside an individual nanorod. Inset: magnified view of the nanorod. **g** Temperature evolution profiles for the Ni$_{0.91}$Mo$_{0.09}$ nanoparticles and MoO$_2$ nanorods inside NiMo-H$_2$ under dark and light conditions. Error bars represent standard deviations from the mean of three tests. Source data are provided as a Source Data file.

of this self-supported catalyst provides more accessible sites for achieving high light absorption. As a result, when light shines on this NiMo-H$_2$ catalyst, the directionally grown MoO$_2$ nanorods act like a forest, allowing light to be absorbed between these nanorods, rather than only at their topmost parts. The abundant Ni$_{0.91}$Mo$_{0.09}$ alloy nanoparticles on these nanorods effectively convert the light into heat, while the dense, micrometer-long MoO$_2$ nanorods, which show slightly higher heat retention ability than the Ni-Mo alloy nanoparticles (Supplementary Fig. S20), help to retain the heat, together resulting in more effective photothermal conversion.

To verify the universality of photothermal-promoted hydrogen production, a series of nickel-based NiX-H$_2$ (X = Co, Fe, V, and W) catalysts exhibiting photothermal effects including NiCo-H$_2$ (Supplementary Fig. S21), NiFe-H$_2$ (Supplementary Fig. S22), NiV-H$_2$ (Supplementary Fig. S23), and NiW-H$_2$ (Supplementary Fig. S24) were synthesized and characterized. UV−vis−NIR spectroscopy analysis and temperature change measurements showed that the NiMo-H$_2$ catalyst has the lowest reflectance over the wavelength range studied (Supplementary Fig. S25) and can reach the highest temperature under identical irradiation conditions (Supplementary Fig. S26), and thus

exhibits the highest photothermal conversion and heat retention capabilities among all these samples.

HER performance in alkaline freshwater

The catalytic performance of these self-supported catalysts was studied under three different conditions: in 1 M KOH freshwater, in 1 M KOH seawater, and in 1 M KOH seawater under light irradiation. To identify the optimal NiMo-H$_2$ catalyst for alkaline HER, a series of NiMo-H$_2$ samples were synthesized by varying the hydrogen reduction temperature over the range from 300 to 600 °C. SEM images in Supplementary Fig. S7 and Supplementary Fig. S27 and TEM images in Supplementary Fig. S8 and Supplementary Fig. S28 show that small-sized Ni-Mo nanoparticles were generated on the surfaces of MoO$_2$ nanorods at a reduction temperature exceeding 400 °C, whereas a high reduction temperature of 600 °C led to surface depressions and a high degree of roughness in the nanorods. Corresponding XRD analysis in Supplementary Fig. S29 reveals that different hydrogen reduction temperatures will result in different compositions of the final product. Among the synthesized NiMo-H$_2$ samples, the one reduced at 500 °C exhibited the highest catalytic activity (Supplementary Fig. S30) and was selected as the representative sample for subsequent testing.

The HER polarization curves in Fig. 3a show that the optimal NiMo-H$_2$ catalyst requires low overpotentials of 33 and 100 mV to reach current densities of 10 and 100 mA cm^{-2} (geometrical area > 0.8 cm^2, scan rate: 1 mV s^{-1}, 90% iR compensation), respectively, in 1 M KOH electrolyte. These values are lower than those for NiMoO$_4$·xH$_2$O (189 and 321 mV) and NiMo-Air (211 and 406 mV). More importantly, the NiMo-H$_2$ catalyst requires only 236 mV to reach a large current density of 500 mA cm^{-2}, which is more meaningful for practical water electrolysis. It also exhibits a smaller Tafel slope value (47.4 mV dec^{-1}, Fig. 3b) compared to that for the NiMoO$_4$·xH$_2$O precursor (110.2 mV dec^{-1}) and for NiMo-Air (160.4 mV dec^{-1}), indicating that a faster transfer coefficient and higher catalytic kinetics can be achieved through hydrogen reduction.

The electrochemically active surface area (ECSA), electrochemical impedance spectroscopy (EIS), and electrochemical activation energy (E_a) for these catalysts were analyzed in depth to better understand the origin of their catalytic differences. The ECSA values for these catalysts were calculated using the electrochemical double-layer capacitance (C_{dl}) method from their CV curves in the non-Faradaic region (Supplementary Fig. S31)[40]. As shown in Supplementary Fig. S31e, the ECSA for NiMo-H$_2$ is calculated to be 485 cm$^2_{ECSA}$, which is 3.6 and 21.6 times
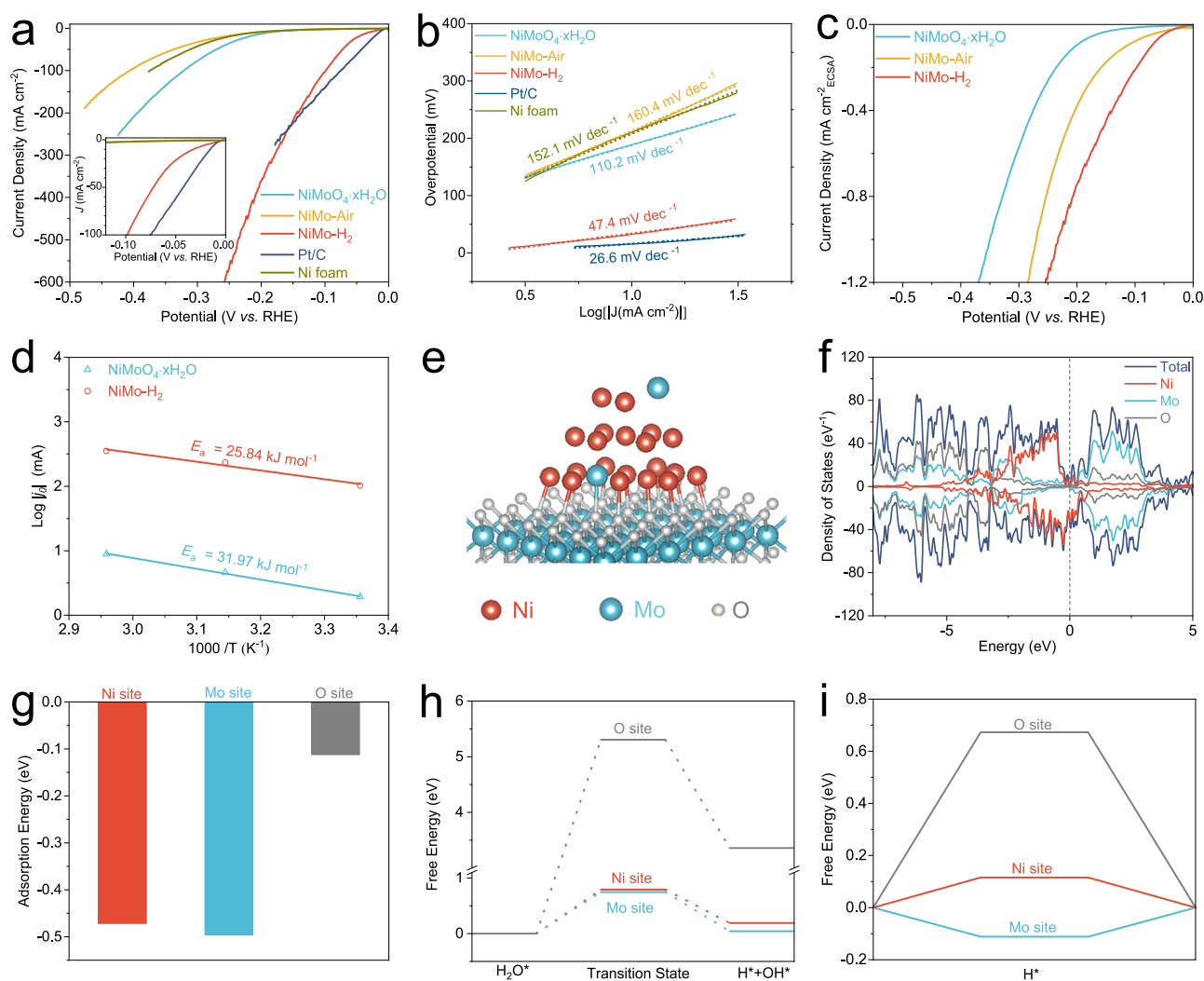
Fig. 3 | Catalytic performance and active sites exploration of catalysts in alkaline freshwater. a HER polarization curves and (**b**) corresponding Tafel plots for NiMoO$_4$·xH$_2$O, NiMo-Air, NiMo-H$_2$, and Pt/C catalysts and Ni foam in 1 M KOH electrolyte. **c** HER polarization curves normalized to ECSA for NiMoO$_4$·xH$_2$O, NiMo-Air, and NiMo-H$_2$ catalysts. **d** Arrhenius plots for NiMoO$_4$·xH$_2$O and NiMo-H$_2$ catalysts. **e** NiMo-H$_2$ model for DFT calculations. **f** DOS plots for the NiMo-H$_2$ model. The gray dashed line indicates the Fermi level. **g** H$_2$O adsorption energy, (**h**) energy diagram for H$_2$O dissociation, and (**i**) free energy diagram for H* adsorption for the Ni, Mo, and O sites in the NiMo-H$_2$ model. Source data are provided as a Source Data file.

that for the NiMoO$_4$·xH$_2$O precursor (135 cm$^2_{ECSA}$) and NiMo-Air (22.5 cm$^2_{ECSA}$), respectively, indicating a notable increase in the number of active sites. When the current density is normalized to ECSA (Fig. 3c), the NiMo-H$_2$ catalyst still demonstrates the highest intrinsic catalytic activity among the catalysts studied, indicating that factors other than ECSA also contribute to the enhancement of its catalytic activity. A catalyst's charge-transfer resistance (R_{ct}) plays an important role in its electrocatalytic reactions. As shown by the EIS results in Supplementary Fig. S32, the R_{ct} value for NiMo-H$_2$ is calculated to be -0.92 Ω, much lower than that for NiMoO$_4$·xH$_2$O (-8.16 Ω). Such a low resistance can be attributed to the metallic properties of the Ni$_{0.91}$Mo$_{0.09}$ nanoparticles and the self-supporting properties of the MoO$_2$ nanorods, both of which facilitate charge transfer kinetics at the electrode-electrolyte interface. In particular, the MoO$_2$ substrate normally has a high conductivity (-6 × 10^3 S cm^{-1})[41,42], which is beneficial for electron transfer to enhance the catalytic reactions. The catalytic activation energy barrier E_a for these catalysts was then calculated based on the Arrhenius equation and their HER polarization curves at different temperatures (Supplementary Fig. S33). As shown in Fig. 3d, the E_a value for NiMo-H$_2$ (25.84 kJ mol^{-1}) is lower than that for the NiMoO$_4$·xH$_2$O precursor (31.97 kJ mol^{-1}), confirming that the hydrogen reduction can reduce the activation energy for HER catalysis.

Theoretical calculations

To gain a better understanding of the catalytic mechanism of the NiMo-H$_2$ catalyst, density functional theory (DFT) simulations were performed. A simplified NiMo-H$_2$ model consisting of a Ni-Mo cluster on a MoO$_2$ substrate was built (Fig. 3e and Supplementary Fig. S34a, b). Charge density difference analysis in Supplementary Fig. S34c,d reveals electron accumulation at the Mo atom in the Ni-Mo cluster (marked by a dashed circle), suggesting the occurrence of electronic structure tuning between the Ni and Mo atoms[43,44]. The density of states (DOS) plots in Fig. 3f show electronic states intersecting the Fermi level, suggesting that the NiMo-H$_2$ catalyst is in the metallic state[45]. For alkaline HER, the NiMo-H$_2$ catalyst (Tafel slope of 47.4 mV dec^{-1}) will first absorb a H$_2$O molecule on its active site (M) and will then follow the Volmer (H$_2$O dissociation, M + H$_2$O + e$^-$→M−H* + OH$^-$)-Heyrovsky (H adsorption/desorption, M − H* + H$_2$O + e$^-$→M + OH$^-$ + H$_2$) procedure to form H$_2$[46–49]. The H$_2$O adsorption energy, the energy barrier for H$_2$O dissociation, and the H* intermediate adsorption energy at the Ni and Mo sites in the Ni-Mo cluster and at the O sites in the MoO$_2$ substrate were all calculated. Detailed reaction pathways are displayed in Supplementary Fig. S35–S37 (Supplementary Data 1). Figure 3g shows that the H$_2$O adsorption energies at the Ni and Mo sites (−0.47 and −0.50 eV, respectively) are much lower than that at the O site (−0.11 eV), which suggests that the metal atoms are more favorable for H$_2$O adsorption. Furthermore, the energy barrier for the subsequent water dissociation (ΔG_{H2O}) step at the Mo site was calculated to be 0.75 eV (Fig. 3h), which is slightly and substantially lower than that at the Ni (0.79 eV) and O (5.30 eV) sites, respectively. Since sluggish water dissociation has been regarded as an additional kinetics-limiting step for alkaline HER, a lower ΔG_{H2O} suggests accelerated H$_2$O dissociation kinetics at the Mo site, which is favorable to the overall HER process[49,50]. The H* adsorption energy (ΔG_{H*}) is the key descriptor for the Heyrovsky step, and optimal catalytic performance is achieved at ΔG_{H*} = 0.0 eV due to the equilibrium between the proton reduction and the removal of adsorbed hydrogen at the active site[48,51]. The ΔG_{H*} at the Mo site was calculated to be −0.11 eV (Fig. 3i), the absolute value of which is slightly lower than that at the Ni site (0.12 eV), suggesting that the Mo site is more favorable for H* adsorption/desorption. Clearly, results from the above theoretical simulations demonstrate that Mo sites have a high capability towards H$_2$O adsorption and dissociation and H* adsorption/desorption, which may contribute to the catalyst's outstanding HER activity[26,52]. These Ni$_{0.91}$Mo$_{0.09}$ nanoparticles were uniformly and densely dispersed on

the MoO$_2$ nanorods in NiMo-H$_2$, effectively exposing the active sites for catalytic reactions. On the other hand, the HER performance of the etched NiMo-H$_2$ sample exhibited a sharp decline (Supplementary Fig. S38), confirming that the Ni-Mo alloy clusters are key to the catalyst's high HER activity.

Thermal management of photothermal electrolyzer

Hydrogen production through seawater electrolysis is attracting increasing research interest due to the inexhaustible reserves of feedstock and abundant offshore renewable energy resources. However, the catalytic performance of catalysts in natural seawater is typically inferior to that in freshwater, resulting in higher energy consumption. As illustrated in Supplementary Fig. S39a, the catalytic activity of all as-synthesized catalysts in 1 M KOH seawater is worse than that in 1 M KOH freshwater, and their corresponding Tafel slope values are generally larger (Supplementary Fig. S39b), which can be attributed to the obstruction of active sites by precipitates, degraded conductivity, and reduced catalytic kinetics in seawater electrolyte[2,6]. Through rational design, the NiMo-H$_2$ catalyst intrinsically possesses a large surface area and high conductivity to reduce the impact of the first two challenges. Given the outstanding photothermal conversion ability of the NiMo-H$_2$ catalyst and the abundant solar energy resources in coastal areas, it would be of great benefit to improve its seawater electrolysis performance through accelerating mass transfer and catalytic kinetics and reducing the activation energy barrier by utilizing photothermal energy. In particular, the temperature increase can accelerate bubble dynamics for gas product release and reduce fluid viscosity to facilitate electrolyte diffusion, thereby accelerating mass transfer to increase the overall reaction rate. In addition, localized heating of the catalyst through the photothermal effect is demonstrably more energy-efficient than heating the entire electrolyzer[53,54]. In other words, the Ni$_{0.91}$Mo$_{0.09}$ nanoparticles, serving as both active sites for the catalytic reaction and effective sites for photothermal conversion, can directly convert solar energy into localized heat to promote the catalytic reaction.

Since a catalyst must be immersed in an electrolyte for a catalytic reaction to occur, there will be massive heat loss at the catalyst-electrolyte interface, leading to poor photothermal utilization. Therefore, optimal photothermal electrolyzer design and thermal management are crucial for assessing the photothermal-promoted catalytic activity of these catalysts[25]. As shown in Supplementary Fig. S40a, we assembled a three-electrode photothermal electrolyzer with a quartz window in front of the catalyst for light harvesting. A piece of low-cost melamine foam (MF) was then placed behind the catalyst to minimize heat diffusion and to create a restricted high-temperature region around the catalyst. MF has high porosity, good hydrophilicity, and low intrinsic thermal conductivity, helping to reduce impacts on electrolyte flow and prevent thermal exchange between the catalyst and the electrolyte. To illustrate the thermal management capability of MF under operating conditions, the temperature evolution of different regions inside this homemade electrolyzer was measured using a thermocouple (Supplementary Fig. S40b–d). When MF is employed as a thermal insulation layer behind the NiMo-H$_2$ catalyst (Supplementary Fig. S40c), the temperature of the region directly facing the light source (T_1) and that behind the catalyst (T_2) can reach as high as -47.2 °C and -41.9 °C, respectively, under simulated one sun irradiation for 1 h, showing good heat preservation with the use of MF. In its absence (Supplementary Fig. S40d), the temperatures at the same locations (T_3 and T_4) under the same irradiation conditions can only reach -38.4 and -36.9 °C, respectively. Considering that these thermocouple-measured temperatures represent those of the bulk electrolyte (Supplementary Fig. S41a,b), we further used a thermal imaging camera to measure the surface temperature of the NiMo-H$_2$ catalyst (Supplementary Fig. S41b,c). As shown in Supplementary Fig. S41b, the temperature of
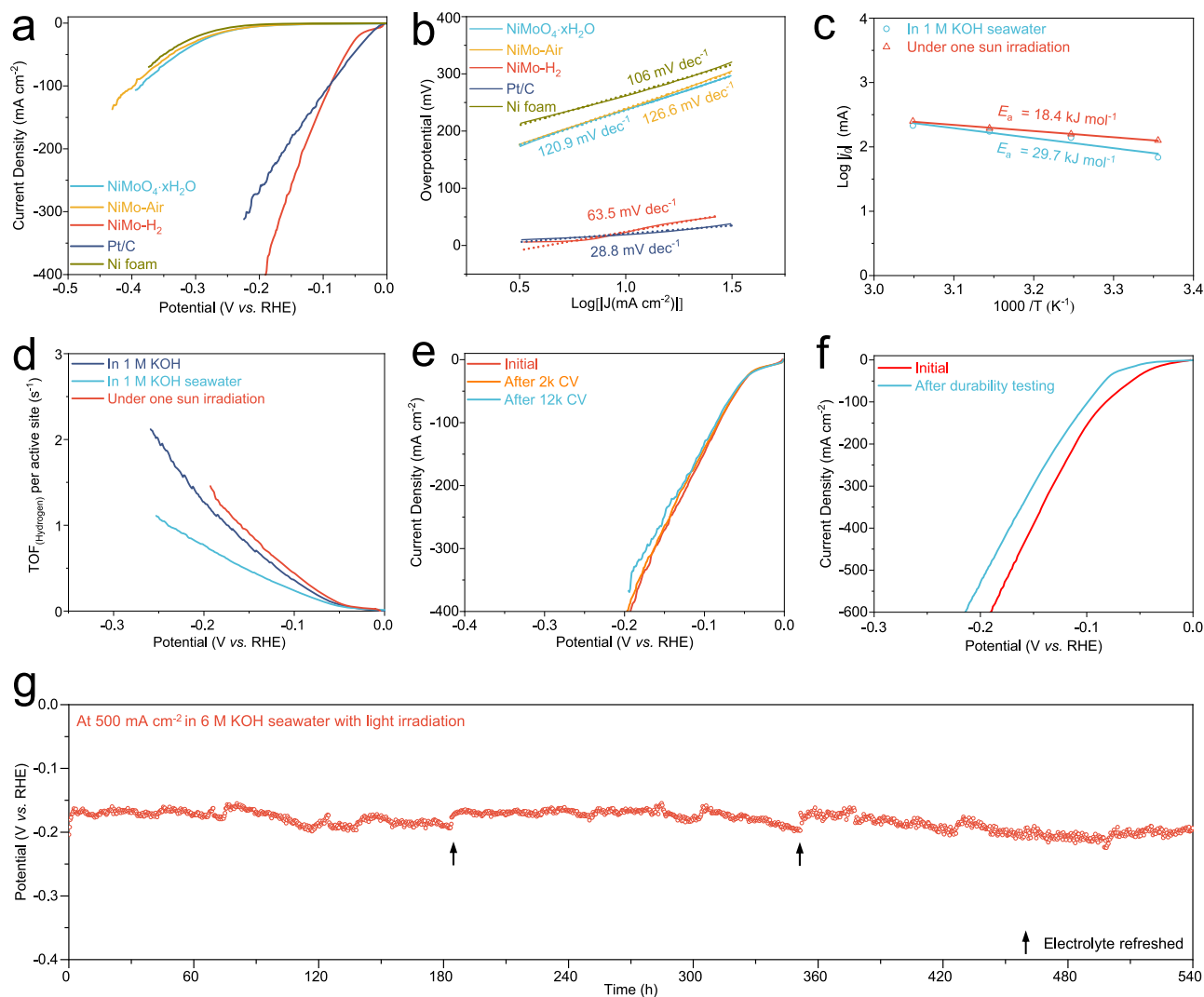
Fig. 4 | Photothermal-promoted Catalytic performance of catalysts in alkaline seawater. a HER polarization curves and (**b**) corresponding Tafel plots for $NiMoO_4 \cdot xH_2O$, NiMo-Air, NiMo-H_2, and Pt/C catalysts and Ni foam in 1 M KOH seawater under simulated one sun irradiation. J is the current density. **c** Arrhenius plots for NiMo-H_2 in 1 M KOH seawater electrolyte. **d** Turnover frequency (TOF) curves for the NiMo-H_2 in 1 M KOH, 1 M KOH seawater, and 1 M KOH seawater under simulated one sun irradiation. **e** HER polarization curves for the NiMo-H_2 catalyst before CV cycling and after different numbers of CV cycles in 1 M KOH seawater under simulated one sun irradiation. **f** HER polarization curves for NiMo-H_2 in 6 M KOH seawater under simulated one sun irradiation before and after long-term durability testing for 540 h. **g** Chronopotentiometric curve for NiMo-H_2 at a constant current density of 500 mA cm^{-2} in 6 M KOH seawater under simulated one sun irradiation. Source data are provided as a Source Data file.

the NiMo-H_2 catalyst surface is clearly higher than that of the nearby electrolyte during the first 15 min of light irradiation, and it remains at least as high as the electrolyte temperature over 60 min of light irradiation. This indicates that the NiMo-H_2 catalyst not only has high photothermal conversion efficiency and can heat up quickly under light irradiation but also maintains a high temperature after transferring heat to the nearby electrolyte. This is because the needle-like structure of NiMo-H_2 allows light to be converted into heat through multiple reflections among its interfaces, while its three-dimensional hollow substrate is conducive to heating the local electrolyte[55].

Insight into photothermal-promoted seawater HER

The photothermal-promoted hydrogen production capability of each studied catalyst was assessed in alkaline natural seawater (1 M KOH seawater). As shown by the HER polarization curves in Fig. 4a, the NiMo-H_2 catalyst requires overpotentials of 23 and 89 mV to reach the current densities of 10 and 100 mA cm^{-2}, respectively, in 1 M KOH seawater under simulated one sun irradiation, which are substantially lower than the corresponding values without light irradiation (36 and 125 mV, Fig S39a). At a given overpotential of 190 mV, the NiMo-H_2 catalyst can reach a large current density of 400 mA cm^{-2} in 1 M KOH seawater under one sun irradiation, which is twice that in 1 M KOH seawater (199 mA cm^{-2}) and even higher than that in 1 M KOH (329 mA cm^{-2}) without photothermal promotion. It also exhibits a small Tafel slope of 63.5 mV dec^{-1} in the photothermal electrolyzer (Fig. 4b). Such notable catalytic performance makes the NiMo-H_2 catalyst comparable to other high-performing alkaline seawater catalysts reported to date (Supplementary Table S1). Supplementary Fig. 42 illustrates the catalytic performance of the NiMo-H_2 catalyst at large current densities in different electrolytes, demonstrating a consistent photothermal enhancement trend in both alkaline freshwater and seawater. It has been demonstrated that the photothermal effect can also enhance catalytic activity in other NiX-H_2 catalysts, all of which achieved higher hydrogen production rates in alkaline seawater under light irradiation (Supplementary Fig. S43a, b). In particular, those catalysts with good photothermal conversation ability (e.g., NiV-H_2,

NiW-H_2, and NiMo-H_2) show more reductions in overpotentials to reach current densities of 10 and 100 mA cm^{-2} (Supplementary Fig. S43c).

In addition to the photothermal conversion ability measurements discussed above, EIS, E_a, and turnover frequency (TOF) analyses were performed to investigate how light irradiation enhances the catalytic activity of the NiMo-H_2 catalyst. The EIS curves in Supplementary Fig. S44 demonstrate that the R_{ct} value for the NiMo-H_2 catalyst in 1 M KOH seawater electrolyte decreased from 3.61 Ω to 2.34 Ω under light irradiation, indicating faster electron and charge transfer. Potential-dependent Bode phase diagrams were constructed to provide further insight into the electrochemical kinetics of NiMo-H_2 during a catalytic reaction (Supplementary Fig. S45). Bode plots describe two electrochemical processes for the catalyst during HER: electron transfer at the interface between the catalyst and the substrate at the high-frequency region (≥1 Hz) and electron transfer from the electrolyte to the catalytic layer at the low-frequency region (<1 Hz)[56]. Under light irradiation, the phase peak angles in the Bode plots are smaller than those for a catalytic reaction without light irradiation at the same applied potentials, as indicated by the dashed arrows in Supplementary Fig. S45, suggesting reduced charge-transfer resistance between the electrolyte and the active sites[57]. Subsequently, the catalytic activation energy barrier E_a for the NiMo-H_2 catalyst in 1 M KOH seawater under different irradiation conditions was calculated using its HER polarization curves at different temperatures (Supplementary Fig. S46). As illustrated in Fig. 4d, the E_a value decreased from 29.7 kJ mol^{-1} without light irradiation to 18.4 kJ mol^{-1} under one sun irradiation, suggesting that the photothermal effect lowers the activation energy for HER catalysis. The TOF, defined as "molecules reacting per active site per unit of time,"[58] was calculated to be ~0.91 s^{-1} for the NiMo-H_2 catalyst at the potential of -0.15 V vs. RHE in 1 M KOH seawater under one sun irradiation (Fig. 4d). This value is around twice that in the absence of light irradiation (-0.48 s^{-1}) and higher than that in 1 M KOH (-0.77 s^{-1}), signifying a higher instantaneous efficiency for the catalytic reaction. These analyses show that, under light irradiation, the NiMo-H_2 catalyst has low charge-transfer resistance, a reduced catalytic activation energy barrier, and high instantaneous efficiency, which together support its good catalytic performance shown in Fig. 4a. In addition to the demonstrated photothermal effect for the NiMo-H_2 catalyst, we also investigated whether it exhibits the photoelectric or photocatalytic effect. As shown in Supplementary Fig. S47, no photocurrent was detected for NiMo-H_2 under chopped full spectrum light irradiation. Likewise, there was no obvious change in its contact potential under either visible or UV light irradiation (Supplementary Fig. S48) and this NiMo-H_2 does not exhibit photocatalytic activity in alkaline electrolytes either (Supplementary Fig. S49). When measured in a cold water environment, where the surrounding temperature remains low and the heat can be rapidly dissipated, there was no obvious difference in catalytic performance when the light is on and off (Supplementary Fig. S50), confirming that light exposure without thermal effect does not enhance performance. Therefore, it can be concluded that the NiMo-H_2 catalyst does not exhibit the photoelectric or photocatalytic effect, leading to the deduction that the enhancement of its catalytic performance under light irradiation stems from the photothermal effect.

Long-term catalytic durability is crucial for catalysts since they must be able to operate at high current densities for extended periods in practical applications. To verify the catalytic durability of the NiMo-H_2 catalyst, HER polarization curves were recorded after multiple cyclic voltammetry (CV) cycles in 1 M KOH seawater under light irradiation. As shown in Fig. 4e, its catalytic activity remained nearly unchanged after 2000 (2k) CV cycles and the overpotential increased slightly even after up to 12k CV cycles, demonstrating the outstanding catalytic durability of this catalyst. When measured at a constant current density of 100 mA cm^{-2} with chopped illumination, the potential

exhibited a rapid and continuous photo-response with good repeatability during each on-off cycle (Supplementary Fig. S51). Since industrial alkaline water electrolysis is performed in highly concentrated OH$^-$ electrolyte, the NiMo-H_2 catalyst was then tested in 6 M KOH seawater electrolyte to assess its photothermal-promoted hydrogen production capability[59,60]. As shown in Fig. 4f, it requires a low overpotential of 171 mV to reach a large current density of 500 mA cm^{-2} in 6 M KOH seawater with the assistance of light irradiation.

In addition to its high intrinsic structural stability due to the alloying effect and the strong interaction between the Ni-Mo alloy nanoparticles and the MoO$_2$ nanorod substrate, the outstanding catalytic durability of the NiMo-H_2 catalyst can be attributed to the thorough distribution of its abundant active sites and its hydrophilic surface. One of the key factors causing catalyst instability at high current densities is a limited number of active sites, which impedes the speed of the catalytic reaction[43,61]. The uniform growth of NiMo-H_2 nanorods with numerous nanoparticle active sites enables the catalytic reaction to take place over the entire surface of the catalyst, overcoming the above challenge. Additionally, synthesis of the NiMo-H_2 catalyst transforms the substrate surface from hydrophobic to hydrophilic (Supplementary Fig. S52), which allows the catalyst to exhibit a low adhesive force for gas bubbles and is advantageous for maintaining long-term catalytic durability[62]. As demonstrated in Supplementary Movie 1, vigorous hydrogen bubbles can be efficiently generated on the surface of the NiMo-H_2 catalyst and released rapidly at a small size, thus minimizing the blocking effect on the active sites and lowering the impact of bubble bursting on resistance and potential fluctuations[63,64]. This is unlike the case of a hydrophobic substrate, where bubbles remain attached to the surface and coalesce into larger-size bubbles before slowly releasing (Supplementary Movie 2). As a result, when measured at a constant current density of 500 mA cm^{-2}, this NiMo-H_2 catalyst suffers a fluctuation in potential of only 66 mV over 540 h of durability testing (Fig. 4g), exhibiting outstanding catalytic durability under strong alkali conditions. After long-term durability testing, it still demonstrated good catalytic activity despite showing an increase in overpotential (Fig. 4f). Corresponding SEM analysis in Supplementary Fig. S53 indicates that although the NiMo-H_2 catalyst experienced structural collapse and crack formation after long-term stability test, a large amount of catalyst still remained on the substrate, indicating good physical stability. When measured at a relatively low current density of 200 mA cm^{-2} for a short time, SEM images in Supplementary Fig. S54 reveal that the original nanorod structure on the substrate was maintained after catalytic durability testing, despite the appearance of some cracks. In-depth inductively coupled plasma (ICP, Supplementary Fig. S55), XPS (Supplementary Fig. S56), Raman (Supplementary Fig. S57), and TEM (Supplementary Fig. S58) analyses together reveal that the NiMo-H_2 catalyst became partially amorphous following long-term durability testing, with the formation of Ni(OH)$_2$ nanoparticles on the nanorods, consistent with previous reports on Ni-Mo based catalysts[28,65–67].
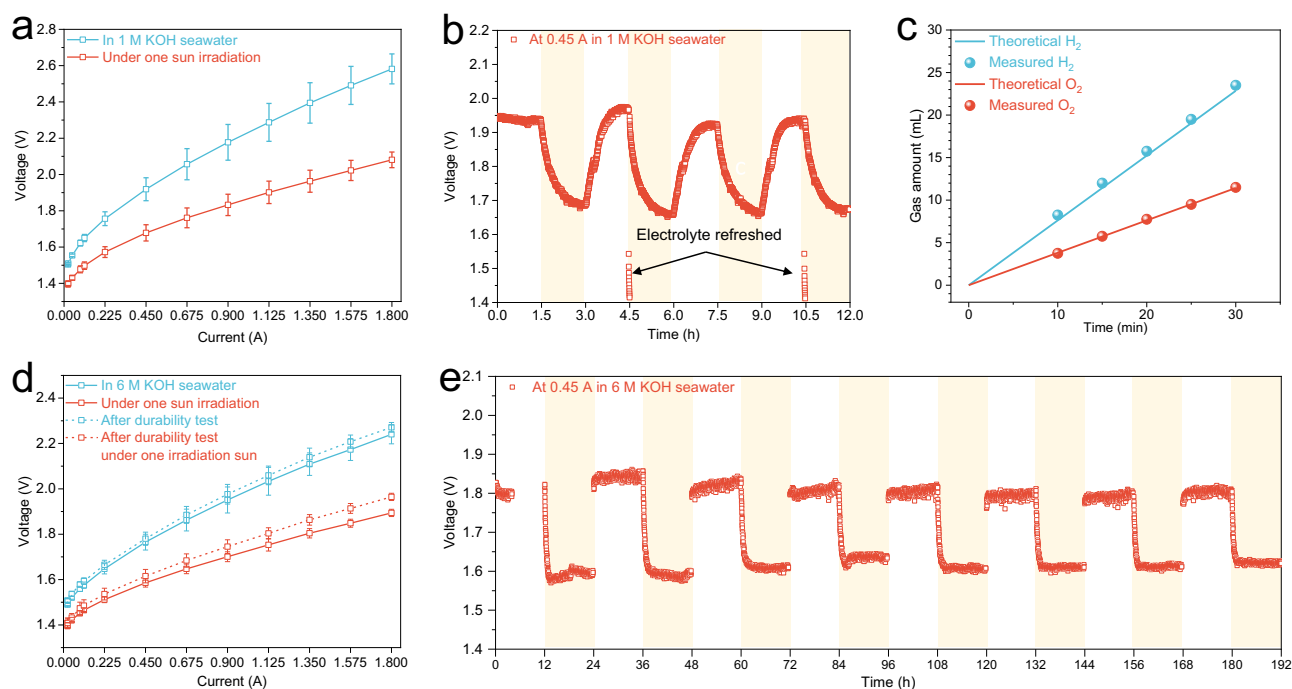
Photothermal-promoted overall AEM seawater electrolysis

There has been no dedicated electrolyzer designed for practical photothermal-promoted overall seawater electrolysis to date, particularly with regard to AEM seawater electrolysis. Apart from the membrane electrode assembly in a traditional AEM electrolyzer, other critical challenges for a photothermal AEM electrolyzer are the efficient utilization of light and the retention of heat. Here we designed and assembled a photothermal AEM electrolyzer (Supplementary Fig. S59) using NiMo-H_2 as the cathode for HER, NiFe LDH (Supplementary Fig. S60) as the anode for OER, and an AEM (Fumasep, FAA-3-PK-130) as the separator. By using transparent coverage, controlling the electrolyte flow rate, and wrapping the electrolyzer with insulation materials, we can effectively utilize light and reduce heat loss. The

working mechanism for this electrolyzer is detailed in Supplementary Fig. S61: when alkaline seawater electrolyte is fed into the electrolyzer, HER and OER occur on the surfaces of the NiMo-H$_2$ and NiFe LDH catalysts, respectively, separated by the intermediate AEM; the generated gas bubbles will flow out through the upper channel into the electrolyte bottle, where the overflowing electrolyte will be collected and recycled; and light irradiation is directed onto the NiMo-H$_2$ catalyst through the transparent cover.

The overall seawater electrolysis performance (without *iR* compensation) of this photothermal AEM electrolyzer was first measured in 1 M KOH seawater electrolyte. For the AEM measurement, the amount of hydrogen produced is determined by the absolute charge transfer amount. To minimize experimental error due to the small catalyst area, the electrode area was set at 1.5 × 1.5 cm, and the absolute current was measured instead of the current density. As shown by the current–voltage curves in Supplementary Fig. S62a, b, and 5a, in the absence of light irradiation, the NiMo-H$_2$||NiFe LDH pair requires voltages of -1.51, -1.76, and -2.58 V to reach currents of 0.0225, 0.225, and 1.8 A, respectively, equivalent to respective current densities of 10, 100, and 800 mA cm^{-2}. Under simulated one sun irradiation, the voltages dropped to -1.40, -1.57, and -2.08 V, respectively, at the same currents (Supplementary Fig. S53c,d and Fig. 5a), indicating that the photothermal effect notably enhanced the catalytic activity. The voltage reduction rates at currents of 0.0225, 0.225, and 1.8 A are 7.3%, 10.8%, and 19.4%, respectively, which proves that the photothermal catalytic enhancement is particularly effective at higher currents. When tested in 1 M KOH, this pair exhibits better performance with a similar photothermal enhancement effect (Supplementary Fig. S63). In addition, while the performance of this NiMo-H$_2$||NiFe LDH pair in the photothermal AEM electrolyzer is lower than that of the traditional titanium alloy AEM electrolyzer under light-free conditions, it surpasses the traditional electrolyzer's performance after being exposed

to light (Supplementary Fig. S64). The Pt/C||NiFe LDH pair was also assembled in the photothermal AEM electrolyzer for comparison, and it shows inferior overall AEM seawater electrolysis performance compared to the NiMo-H$_2$||NiFe LDH pair under both light-off and light-on conditions (Supplementary Fig. S65). In particular, the voltage drop of the Pt/C||NiFe LDH pair under light on is smaller than that of the NiMo-H$_2$||NiFe LDH pair due to the inferior photothermal effect of the Pt/C electrode. When measured at a constant current of 0.45 A under chopped illumination, this photothermal AEM electrolyzer exhibits a good photothermal response, with a rapid and notable drop in voltage upon lamp activation (Fig. 5b). The Faradaic efficiency for photothermal-promoted overall seawater electrolysis was measured using a H-type electrolyzer (Supplementary Fig. S66). The results in Fig. 5c show that the amount of gas produced closely matches theoretical expectations, confirming high Faradaic efficiency and the absence of chlorine evolution reaction. The NiMo-H$_2$||NiFe LDH pair was additionally tested in 6 M KOH seawater electrolyte, which simulates an industrial strong alkaline environment, to evaluate its effectiveness under harsher conditions. As shown in Fig. 5d, it requires voltages of only -1.40, -1.51, and -1.80 V to reach currents of 0.0225, 0.225, and 1.8 A in 6 M KOH seawater under simulated one sun irradiation, considerably lower than the corresponding voltages required without light irradiation. Catalytic durability, which is crucial in practical applications, was further tested by operating the NiMo-H$_2$||NiFe LDH pair in 6 M KOH seawater at a constant current of 0.45 A with alternating on-off cycles of illumination every 12 h. As shown in Supplementary Fig. S67 and Fig. 5e, the required voltage can be reduced by -0.22 V, from -1.82 V to -1.60 V, with the assistance of light irradiation, demonstrating good catalytic repeatability over 192 h of durability testing. Supplementary Movie 3 shows effective and stable operation with vigorous bubble generation at high current, highlighting the potential for practical photothermal-promoted hydrogen production

Fig. 5 | Photothermal-promoted AEM seawater electrolysis. a Overall seawater electrolysis performance by the NiMo-H$_2$||NiFe LDH pair in 1 M KOH seawater with and without light irradiation. Error bars represent standard deviations from the mean of the tests. **b** Chronopotentiometric curve for the NiMo-H$_2$||NiFe LDH pair at a constant current of 0.45 A in 1 M KOH seawater under off and on cycles of illumination. Yellow regions represent durations of time when the light is on. **c** Measured (dots) and theoretical (solid lines) gaseous products from overall

seawater electrolysis using the NiMo-H$_2$||NiFe LDH pair. **d** Overall seawater electrolysis performance by the NiMo-H$_2$||NiFe LDH pair in 6 M KOH seawater with and without light irradiation before and after durability testing. Error bars represent standard deviations from the mean of the tests. **e** Chronopotentiometric curve for the NiMo-H$_2$||NiFe LDH pair at a constant current of 0.45 A in 6 M KOH seawater off and on cycles of illumination. Yellow regions represent durations of time when the light is on. Source data are provided as a Source Data file.

from seawater electrolysis. Accordingly, the energy efficiency of this photothermal AEM electrolyzer was calculated to be ~76.8% under light irradiation and the corresponding energy consumption for seawater hydrogen production is 3.83 kW·h/Nm³ (Supplementary Note 1). While most works in seawater electrolysis field are focusing on catalyst exploration and tested in traditional AEM electrolyzer (Supplementary Table S3), the NiMo-H_2||NiFe LDH pair in photothermal AEM electrolyze shows comparable and, in some cases, better performance. After the 8-day durability test, the voltages required to reach currents of 0.0225, 0.225, and 1.8 A under simulated one sun irradiation increased by ~0.01, ~0.03, and ~0.06 V, respectively, for respective total required voltages of ~1.41, ~1.54, and ~1.86 V (Supplementary Fig. S68), still showcasing notable photothermal-promoted overall seawater electrolysis performance by the NiMo-H_2||NiFe LDH pair. When measured at a constant current of 0.12 A (Supplementary Fig. S69), this system operated for over 800 h (34 d), demonstrating good durability and feasibility. Additionally, we also performed outdoor experiment using this photothermal AEM electrolyzer powered by a commercial solar cell. As shown in Supplementary Fig. S70, this system can deliver a current of ~0.61 A with an operating voltage of ~1.8 V with photothermal effect under a solar intensity of 69.6 mW cm⁻², indicating a high potential for seawater hydrogen production with zero carbon emissions.

Discussion

To design a seawater electrolysis system that can effectively utilize external renewable energy, e.g. the clean and free solar energy available in offshore areas, an active and durable NiMo-H_2 catalyst was explored for photothermal-promoted HER. This catalyst is composed of $Ni_{0.91}Mo_{0.09}$ nanoparticles generated in situ on MoO_2 nanorods and its hierarchical structure provides rich accessible reactive sites for catalytic reactions and exhibits high light absorption and photothermal conversion capabilities. Apart from the structural design, the alloying in this catalyst endows it with high structural stability and rapid electron transfer, which enable it to work stably under seawater conditions. DFT calculations indicate that the Mo sites in the $Ni_{0.91}Mo_{0.09}$ nanoparticles should be active sites for catalytic reactions due to their rapid dissociation kinetics and low hydrogen adsorption energies. Various characterizations verified that these bimetallic $Ni_{0.91}Mo_{0.09}$ nanoparticles are also effective sites for photothermal conversion, which can directly convert solar energy into thermal energy to promote catalytic reactions. As a result, under simulated one sun irradiation, the NiMo-H_2 catalyst achieves a current density of 400 mA cm⁻² at an overpotential of merely 190 mV in 1 M KOH seawater and maintains good durability over 540 h of operation at 500 mA cm⁻² in 6 M KOH seawater. When coupled with the OER-active NiFe LDH catalyst in a photothermal AEM electrolyzer, the NiMo-H_2||NiFe LDH pair requires a voltage of only ~1.6 V to drive a current of 0.45 A under simulated one sun irradiation, demonstrating outstanding repeatability over 192 h of durability testing. In terms of potential scenarios, this technology can facilitate hydrogen production in coastal or offshore areas, decentralized hydrogen production driven by renewable energy, and hydrogen production in areas with abundant photothermal energy but low water quality. To promote the potential application of this system, possible technical challenges in scaling up and electrolyzer stack design should be considered. For example, addressing the challenges in electrolyzer scaling up requires attention to catalyst uniformity, light and heat management, as well as electrolyte/gas flow control. To assemble a tightly packed electrolyzer stack that enhances reaction efficiency, the light path needs to be carefully designed to optimize light delivery and distribution within the system by integrating a tailored optical setup into each individual electrolyzer to ensure localized heating of the catalyst. In general, most studies on seawater electrolysis have been performed using conventional three-electrode or two-electrode AEM electrolyzer. Our

work not only explores and studies a multifunctional NiMo-H_2 catalyst but also designs and develops a photothermal-promoted AEM electrolyzer, offering insights into the design of seawater electrolysis systems.

Methods

Synthesis of NiMoO₄·xH₂O precursor

Self-supported $NiMoO_4·xH_2O$ precursors were grown in situ on the surface of conductive substrates [nickel foam (NF) or copper foam (CF)] via a water bath reaction based on our previous work[34]. Briefly, a piece of substrate (1.5 cm × 3.5 cm) was first cleaned by HCl solution, ethanol, and deionized (DI) water with the assistance of sonication. Afterward, 2 mmol nickel nitrate hexahydrate [Ni(NO₃)₂·6H₂O, 99%, Acros Organics], 0.25 mmol ammonium molybdate tetrahydrate [(NH₄)₆Mo₇O₂₄·4H₂O, 81–83% MoO₃ basis, Sigma Aldrich], and 3 mmol urea [CO(NH₂)₂, 99.5%, Sigma Aldrich] were dissolved in 20 mL DI water in a glass bottle with stirring. The clean substrate was placed in the bottle, which was then transferred to a water bath oven maintained at 90 °C for 8 h. After the reaction was completed, the resulting self-supported $NiMoO_4·xH_2O$ precursor was rinsed several times with DI water and dried in air. Powdered $NiMoO_4·xH_2O$ samples were obtained by collecting and drying the precipitate peeled off from the substrate.

Synthesis of NiMo-H₂ and NiMo-Air catalysts

The nanorod-nanoparticle-structured NiMo-H_2 catalyst was synthesized through hydrogen reduction of the as-prepared $NiMoO_4·xH_2O$ precursor. Typically, the self-supported $NiMoO_4·xH_2O$ precursor was reduced in a quartz tube at 500 °C for 2 h under a mixed hydrogen-nitrogen (4–96%) gas flow. After naturally cooling down, the black product was denoted NiMo-H_2. To determine the optimal hydrogen reduction temperature, other NiMo-H_2 catalysts were prepared through a similar procedure except for varying the reduction temperature over the range from 300 to 600 °C. For comparison, a NiMo-Air catalyst was prepared via annealing the self-supported $NiMoO_4·xH_2O$ precursor in a muffle furnace at 700 °C for 2 h in air. Powdered NiMo-H_2 and NiMo-Air samples were prepared through the same respective procedures, except that powdered $NiMoO_4·xH_2O$ was used in place of the self-supported $NiMoO_4·xH_2O$ precursor.

Synthesis of NiX-H₂ (X = Co, Fe, V, and W) catalysts

A series of nickel-based NiX-H_2 catalysts (X = Co, Fe, V, and W) were synthesized through a procedure similar to that used for NiMo-H_2 for comparison. In detail, Ni-X layered double hydroxide (NiX LDH) precursors were first synthesized[68–71], and a hydrogen reduction process was then performed at 500 °C for 2 h to obtain each NiX-H_2 catalyst. To maintain their original structure, NiCo-H_2 and NiFe-H_2 catalysts were each prepared at a lower reduction temperature of 400 °C.

Preparation of Pt/C electrode

A Pt/C electrode was prepared to serve as the benchmark HER catalyst for comparison. Briefly, 50 mg commercial platinum on carbon powder (Pt/C, 20% on carbon, Sigma Aldrich) was homogenously dissolved in a mixture solution containing 1600 μL ethanol, 200 μL Nafion 117 solution (5%, Sigma Aldrich), and 1200 μL DI water with the assistance of ultrasonication. A piece of clean NF substrate (3 cm²) was soaked in the solution, sonicated for 1.5 h, and then dried in an oven.

Materials characterization

The morphology and elemental distribution of the as-prepared samples were studied using scanning electron microscopy (SEM, JEOL FEG JSM 7001 F) and transmission electron microscopy (TEM, JEOL 2100 F) with energy-dispersive X-ray spectroscopy (EDS). The crystal structure and composition were identified using X-ray diffraction (XRD, 5005 Bruker X-ray diffractometer, Cu Kα radiation). The valence state was

determined by X-ray photoelectron spectroscopy (XPS, Kratos AXIS Ultra, mono Al Kα X-ray source). Raman tests were conducted using a Renishaw inVia Raman microscope (laser wavelength: 532 nm). The reflectance spectra were obtained using an ultraviolet–visible–near-infrared (UV–vis–NIR) spectrophotometer (UV-3600, Shimadzu). The infrared images were captured using an infrared camera (E50, FLIR). Atomic force microscopy (AFM), Kelvin probe force microscopy (KPFM), and scanning thermal microscopy (SThM) measurements were carried out on a commercial scanning probe microscopy (SPM) system (MFP-3D, Asylum Research, Oxford Instruments). The metallic cation concentration before and after testing was measured using an inductively coupled plasma-optical emission spectrometer (ICP-OES, PerkinElmer Avio 500). Photocatalytic activity was measured using a gas chromatography (Shimadzu, GC-2014AT). The Ni K-edge X-ray absorption find structure spectra of the NiMo-H$_2$ catalyst and standard samples (Ni foil and NiO) were collected via easyXAF300+ (easyXAFS, USA) in transmission mode and all spectra were collected in ambient conditions at room temperature.

Electrochemical characterization

The catalytic performance of the as-prepared catalysts was measured on an electrochemical station (SP150e, BioLogic) using a three-electrode configuration at room temperature. The self-supported catalyst (geometric surface area in the electrolyte > 0.8 cm^2), a Hg/HgO electrode, and a carbon rod were used as the working, reference, and counter electrodes, respectively. After stabilization, each HER polarization curve was recorded at a scan rate of 1 mV s^{-1} with 90% iR compensation. The measured potential ($E_{Hg/HgO}$) was calibrated to the reversible hydrogen electrode (RHE) using the equation: $E_{RHE} = E_{Hg/HgO} + 0.098 + 0.0591 \times pH$. The theoretical pH value of 1 M KOH is 14. The Tafel slope (b) was calculated using the equation $\eta = a + b \log(j)$, where η is the overpotential and j is the current density. For the photothermal-promoted catalytic reaction, full spectrum light from a 300 W Xe lamp (CEL-PE300E-3A) with an intensity of 100 mW cm^{-2} (simulated one sun irradiation) was applied to the catalyst in a homemade photothermal electrolyzer (Supplementary Fig. S40a, the electrolyte volume is around 30 mL). Electrochemical impedance spectroscopy (EIS) was measured at a constant potential of -0.2 V vs. RHE with varied frequency from 100 kHz to 0.1 Hz. The electrochemically active surface area (ECSA) was calculated through the double-layer capacitance (C_{dl}) method. Briefly, cyclic voltammetry (CV) cycling was performed in a non-Faradaic region with different scan rates and the C_{dl} was then obtained as half of the slope in the plot of capacitive current as a function of scan rate. ECSA was calculated from the equation: ECSA = C_{dl}/C_s, where C_s is the specific capacitance (40 μF cm^{-2}). For CV durability testing, CV cycling was performed between 0 and −0.2 V vs. RHE with a scan rate of 100 mV s^{-1}. Chronopotentiometric measurement was carried out at a current density of 500 mA cm^{-2} in 6 M KOH seawater electrolyte under one sun irradiation and the electrolyte was renewed over intervals of ~7 days. Due to the continuous consumption and evaporation of the electrolyte, 0.1 M KOH seawater solution was added at a rate of ~0.25 mL h^{-1} using a peristaltic pump. Overall seawater electrolysis testing was performed in a homemade photothermal anion exchange membrane (AEM) electrolyzer with NiMo-H$_2$ as the cathode (area: 2.25 cm^2), NiFe LDH as the anode, and an AEM (Fumasep FAA-3-PK-130, thickness 130 μm) as the separator. The membrane was immersed in 0.5 M NaCl solution for 24 h for activation. Two peristaltic pumps were used to feed the electrolyte. A DC power station was used to supply the current and a multimeter (Keithley DMM6500) was used to record the real-time voltage. For long-term overall seawater electrolysis durability testing, the photothermal AEM electrolyzer was measured at a constant current of 0.45 A with the lamp alternately switched on or off every ~12 h. (It should be noted that there is no iR compensation for the results from overall seawater electrolysis testing.) Natural seawater was collected from Straits of Singapore, Sentosa, Singapore (1.248° N, 103.822° E). To prevent alkali metal precipitates from adhering to the membrane and thus hindering anion exchange, the Mg^{2+} and Ca^{2+} cations in the natural seawater were removed by adding 0.68 g Na$_2$CO$_3$ into 100 mL natural seawater before preparing alkaline seawater electrolyte.

Calculation of TOF

The turnover frequency (TOF) value for the NiMo-H$_2$ HER catalyst was estimated using the following equation[72,73]:

$$TOF = \frac{Number\,of\,total\,hydrogen\,turnovers/geometrical\,area\,(cm^2)}{Number\,of\,surface,\,active\,sites/geometrical\,area\,(cm^2)} \quad (1)$$

The total number of hydrogen turn overs:

$$Number\,of\,H_2 = \left(j\frac{A}{cm^2}\right)\left(\frac{1\,C\,s^{-1}}{1000\,mA}\right)\left(\frac{6.02\times10^{23}\,H_2\,molecules}{1\,mol\,H_2}\right)\left(\frac{1\,mol\,e^-}{96485.3\,C}\right)\left(\frac{1\,mol\,H_2}{2\,mol\,e^-}\right)$$

$$= 3.12\times10^{15}\,\frac{H_2\,s^{-1}}{cm^2}\,per\,\frac{mA}{cm^2}$$

It should be noted that, since the nature of the surface-active sites is not yet understood and the exact number of hydrogen binding sites is not known, we estimated the number of active sites as the total number of the surface sites from the roughness factor together with the unit cell of the catalysts, which may underestimate the actual TOF. Thus, the upper limit of the active sites for NiMo-H$_2$ (including all Ni, Mo, and O atoms and assuming that the number of active sites is the same for Ni$_{0.91}$Mo$_{0.09}$ and MoO$_2$) per unit of actual surface area can be calculated using the following equations:

$$Number\,of\,active\,sites = \left(\frac{Number\,of\,atoms/unit\,cell}{Volume/unit\,cell}\right)^{2/3} \quad (2)$$

$$Number\,of\,active\,sites\,(MoO_2) = \left(\frac{3\,atoms/unit\,cell}{32.95\,Å^3/unit\,cell}\right)^{2/3} = 2.02\times10^{15}\,atoms\,cm^{-2}$$

$$Number\,of\,active\,sites\,(Ni_{0.91}Mo_{0.09}) = \left(\frac{3\,atoms/unit\,cell}{45.3\,Å^3/unit\,cell}\right)^{2/3} = 1.64\times10^{15}\,atoms\,cm^{-2}$$

As a result, the upper limit for the number of active sites for NiMo-H$_2$ is around 1.83×10^{15} atoms cm^{-2}. The plots of current density can be converted into TOF plots using the equation:

$$TOF_{HER} = \frac{3.12\times10^{15}\,\frac{H_2\,s^{-1}}{cm^2}\,per\,\frac{mA}{cm^2}\times j}{Number\,of\,active\,sites\times A_{ECSA}}$$

Faradaic efficiency measurement

The Faradaic efficiency (FE) of the NiMo-H$_2$||NiFe LDH pair for photothermal-promoted overall alkaline seawater electrolysis was evaluated using a sealed H-type electrolyzer through a drainage method. A constant current of 100 mA was applied to the electrolyzer in 1 M KOH seawater and then the volume (V) of gas products was recorded every 5 min. FE was calculated based on the equation:

$$FE = \frac{V}{(V_m \times i \times t)/(n \times F)} \times 100\% \quad (3)$$

in which V is the collected gas volume (L), V$_m$ is the standard molar volume at room temperature (~24.5 L mol^{-1}), i represents the applied current (A), t is the duration of electrolysis (s), n is the number of electrons required per gas molecule formed (2 for H$_2$ gas and 4 for O$_2$ gas), and F is the Faraday constant (96485.3 C mol^{-1}).

Theoretical calculation

Density functional theory (DFT) calculations were performed using the Vienna ab initio simulation package (VASP) code under the generalized gradient approximation (GGA) combined with the Perdew-Burke-Ernzerhof (PBE) functional. The cut-off energy for the plane-wave basis was set to 450 eV. The DFT + U method was used to introduce Mo processing highly localized 3 d states using the parameter U · J = 4.38 eV. The Van der Waals (vdW) interaction was described by using the empirical correction in Grimme's scheme (DFT-D3) in all calculations. All structures were fully optimized until the energy and force were less than 10^{-5} eV and 0.05 eV/Å, respectively. The unit cell of the NiMo-H_2 catalyst was constructed using a Ni-Mo alloy cluster on MoO_2 (Supplementary Fig. S34a-b) based on the structural and compositional characterizations and taking into account thermodynamic stability. However, it should be noted that the calculation model may not strictly represent real experimental conditions due to the difficulties in modeling. The MoO_2 (101) plane was modeled by building a $6 \times 6 \times 1$ supercell and a vacuum space of 15 Å along the z-axis was added to avoid interactions between periodic images. As shown in Supplementary Fig. S35-S37, Ni and Mo sites in the Ni-Mo cluster and O sites in the MoO_2 are exposed for DFT calculations. For alkaline HER of this NiMo-H_2 catalyst (Tafel slope is 47.4 mV dec^{-1}), the reactant (H_2O) is first adsorbed on active sites (M) and then dissociates into intermediates (OH$^-$ and M-H*) via the Volmer reaction. Subsequently, the hydrogen will be desorbed via the Heyrovsky reaction, in which another H_2O molecule and an extra electron will diffuse to M-H* and form H_2 and OH$^-$. The climbing-image nudged elastic band (CI-NEB) method was applied to evaluate the H_2O decomposition barrier[74,75]. All transition states were verified by vibration analyses with only one imaginary frequency. The H_2O adsorption energy (E_{ads}) was defined as: $E_{ads} = E_{total} - E_{substrate} - E_{H2O}$, where a more negative E_{ads} generally indicates stronger adsorption. In this equation, E_{total}, $E_{substrate}$, and E_{H2O} are the total energies of the H_2O adsorption on the substrate, the energy of the substrate, and the energy of the H_2O, respectively. The Gibbs free energy (ΔG_{*H}) of hydrogen adsorption at 300 K was calculated by: $\Delta G_{*H} = E_{*+H} - E_* - 0.5E_{H2} + 0.24$, where E_* and E_{*+H} are the total energy of the substrate and hydrogen adsorption on the substrate surface, respectively, and E_{H2} is the DFT-calculated total energies of gaseous hydrogen.

Data availability

All data within the article and the Supplementary Information that support the findings of this study are available, or from the corresponding author upon request. Source data are provided with this paper.

References

1. Staffell, I. et al. The role of hydrogen and fuel cells in the global energy system. *Energy Environ. Sci.* **12**, 463–491 (2019).
2. Kuang, Y. et al. Solar-driven, highly sustained splitting of seawater into hydrogen and oxygen fuels. *Proc. Natl Acad. Sci. USA.* **116**, 6624–6629 (2019).
3. Tong, W. et al. Electrolysis of low-grade and saline surface water. *Nat. Energy* **5**, 367–377 (2020).
4. Bennett, J. E. et al. Electrodes for generation of hydrogen and oxygen from seawater. *Int. J. Hydrog. Energy* **5**, 401–408 (1980).
5. Jin, H. et al. Emerging materials and technologies for electrocatalytic seawater splitting. *Sci. Adv.* **9**, eadi7755 (2023).
6. Yu, L. et al. Non-noble metal-nitride based electrocatalysts for high-performance alkaline seawater electrolysis. *Nat. Commun.* **10**, 5106 (2019).
7. Sun, F. et al. Energy-saving hydrogen production by chlorine-free hybrid seawater splitting coupling hydrazine degradation. *Nat. Commun.* **12**, 4182 (2021).
8. Dresp, S. et al. Direct electrolytic splitting of seawater: opportunities and challenges. *ACS Energy Lett.* **4**, 933–942 (2019).
9. Yu, Z. Y. et al. Clean and affordable hydrogen fuel from alkaline water splitting: past, recent progress, and future prospects. *Adv. Mater.* **33**, e2007100 (2021).
10. Hu, H. et al. Metal nitrides for seawater electrolysis. *Chem. Soc. Rev.* **53**, 163–203 (2024).
11. Lagadec, M. F. et al. Water electrolysers with closed and open electrochemical systems. *Nat. Mater.* **19**, 1140–1150 (2020).
12. Dionigi, F. et al. Design criteria, operating conditions, and nickel-iron hydroxide catalyst materials for delective deawater rlectrolysis. *ChemSusChem* **9**, 962–972 (2016).
13. Liu, J. et al. Rationally designing efficient electrocatalysts for direct seawater splitting: challenges, achievements, and promises. *Angew. Chem., Int. Ed.* **61**, e202210753 (2022).
14. Zhang, F. et al. Rational design of oxygen evolution reaction catalysts for seawater electrolysis. *Trends Chem.* **3**, 485–498 (2021).
15. Liang, J. et al. Electrocatalytic seawater splitting: Nice designs, advanced strategies, challenges and perspectives. *Mater. Today* **69**, 193–235 (2023).
16. Fei H. et al. Direct seawater electrolysis: from catalyst design to device applications. *Adv. Mater.* **36**, 2309211 (2024).
17. Veroneau S. S. et al. Continuous electrochemical water splitting from natural water sources via forward osmosis. *Proc. Natl. Acad. Sci.* **118**, e2024855118 (2021).
18. Veroneau, S. S. et al. Direct seawater splitting by forward osmosis coupled to water electrolysis. *Acs. Appl. Energy Mater.* **5**, 1403–1408 (2022).
19. Xie, H. et al. A membrane-based seawater electrolyser for hydrogen generation. *Nature* **612**, 673–678 (2022).
20. Marin, D. H. et al. Hydrogen production with seawater-resilient bipolar membrane electrolyzers. *Joule* **7**, 765–781 (2023).
21. Cui, X. et al. Photothermal nanomaterials: a powerful light-to-heat converter. *Chem. Rev.* **123**, 6891–6952 (2023).
22. Wang, W. et al. Photothermal-enabled single-atom catalysts for high-efficiency hydrogen peroxide photosynthesis from natural seawater. *Nat. Commun.* **14**, 2493 (2023).
23. Menzinger, M. et al. The meaning and use of the Arrhenius activation energy. *Angew. Chem., Int. Ed.* **8**, 438–444 (1969).
24. Gao L. et al. Operando unraveling photothermal-promoted dynamic active-sites generation in $NiFe_2O_4$ for markedly enhanced oxygen evolution. *Proc. Natl. Acad. Sci. USA.* **118**, (2021).
25. Meng, F. L. et al. A hybrid solar absorber-electrocatalytic N-doped carbon/alloy/semiconductor electrode for localized photothermic electrocatalysis. *Adv. Mater.* **31**, e1903605 (2019).
26. Zhang, J. et al. Efficient hydrogen production on $MoNi_4$ electrocatalysts with fast water dissociation kinetics. *Nat. Commun.* **8**, 15437 (2017).
27. Chen Y. Y. et al. Self-templated fabrication of $MoNi_4/MoO_{3-x}$ nanorod arrays with dual active components for highly efficient hydrogen evolution. *Adv. Mater.* **29**, (2017).
28. Luo, M. et al. Insights into alloy/oxide or hydroxide interfaces in Ni-Mo-based electrocatalysts for hydrogen evolution under alkaline conditions. *Chem. Sci.* **14**, 3400–3414 (2023).
29. Durr, R. N. et al. From $NiMoO_4$ to gamma-NiOOH: detecting the active catalyst phase by time resolved in situ and operando Raman spectroscopy. *ACS Nano* **15**, 13504–13515 (2021).
30. Patil, R. B. et al. Direct observation of Ni–Mo bimetallic catalyst formation via thermal reduction of nickel molybdate nanorods. *ACS Catal.* **10**, 10390–10398 (2020).
31. Tsurov, M. A. et al. Composition and catalytic properties of products from the reduction of $NiMoO_4$. *Appl. Catal. A: Gen.* **105**, 205–221 (1993).

32. Liu, X. et al. Upraising the O 2p orbital by integrating Ni with MoO$_2$ for accelerating hydrogen evolution kinetics. *ACS Catal.* **9**, 2275–2285 (2019).

33. Zhai, P. et al. Regulating electronic states of nitride/hydroxide to accelerate kinetics for oxygen evolution at large current density. *Nat. Commun.* **14**, 1873 (2023).

34. Wu, L. et al. Efficient alkaline water/seawater hydrogen evolution by a nanorod-nanoparticle-structured Ni-MoN catalyst with fast water-dissociation kinetics. *Adv. Mater.* **34**, e2201774 (2022).

35. Zhai, P. et al. Engineering active sites on hierarchical transition bimetal oxides/sulfides heterostructure array enabling robust overall water splitting. *Nat. Commun.* **11**, 5462 (2020).

36. Duan, Y. et al. Bimetallic nickel-molybdenum/tungsten nanoalloys for high-efficiency hydrogen oxidation catalysis in alkaline electrolytes. *Nat. Commun.* **11**, 4789 (2020).

37. Wang, M. et al. Alloying nickel with molybdenum significantly accelerates alkaline hydrogen electrocatalysis. *Angew. Chem., Int. Ed.* **60**, 5771–5777 (2021).

38. Du, W., Shi, Y., Zhou, W., Yu, Y. & Zhang, B. Unveiling the in situ dissolution and polymerization of Mo in Ni$_4$Mo alloy for promoting the hydrogen evolution reaction. *Angew. Chem., Int. Ed.* **60**, 7051–7055 (2021).

39. Ng, S. W. L. et al. Localized ultrafine Cu clusters within MOF-derived metal oxides for collective photochemical and photothermal H$_2$ generation. *Appl. Catal. B: Environ.* **340**, 123182 (2024).

40. Yilmaz G. et al. Functional defective metal-organic coordinated network of mesostructured nanoframes for enhanced electrocatalysis. *Adv. Funct. Mater.* **28**, (2017).

41. Shi, Y. et al. Ordered mesoporous metallic MoO$_2$ materials with highly reversible lithium storage capacity. *Nano Lett.* **9**, 4215–4220 (2009).

42. Xie Q. et al. High electrical conductivity of individual epitaxially grown MoO$_2$ nanorods. *Appl. Phys. Lett.* **111**, (2017).

43. Jiao, S. et al. Perfecting electrocatalysts via imperfections: towards the large-scale deployment of water electrolysis technology. *Energy Environ. Sci.* **14**, 1722–1770 (2021).

44. Yao, Y. et al. Interfacial sp C-O-Mo hybridization originated high-current density hydrogen evolution. *J. Am. Chem. Soc.* **143**, 8720–8730 (2021).

45. Miao, L. et al. Computational chemistry for water-splitting electrocatalysis. *Chem. Soc. Rev.* **53**, 2771–2807 (2024).

46. Skúlason, E. et al. Nanoscale nickel oxide/nickel heterostructures for active hydrogen evolution electrocatalysis. *J. Phys. Chem. C.* **114**, 18182–18197 (2010).

47. Gong, M. et al. Nanoscale nickel oxide/nickel heterostructures for active hydrogen evolution electrocatalysis. *Nat. Commun.* **5**, 4695 (2014).

48. Liu, B. et al. Unconventional nickel nitride enriched with nitrogen vacancies as a high-efficiency electrocatalyst for hydrogen evolution. *Adv. Sci. (Weinh.)* **5**, 1800406 (2018).

49. Sun, F., Tang, Q. & Jiang, D.-e Theoretical Advances in Understanding and Designing the Active Sites for Hydrogen Evolution Reaction. *ACS Catal.* **12**, 8404–8433 (2022).

50. Wu X. et al. Engineering multifunctional collaborative catalytic interface enabling efficient hydrogen evolution in all pH range and seawater. *Adv. Energy Mater.* **9**, (2019).

51. Lu, Q. et al. Highly porous non-precious bimetallic electrocatalysts for efficient hydrogen evolution. *Nat. Commun.* **6**, 6567 (2015).

52. Bau, J. A. et al. Role of oxidized Mo species on the active surface of Ni–Mo electrocatalysts for hydrogen evolution under alkaline conditions. *ACS Catal.* **10**, 12858–12866 (2020).

53. Gao, M., Zhang, T. & Ho, G. W. Advances of photothermal chemistry in photocatalysis, thermocatalysis, and synergetic photothermocatalysis for solar-to-fuel generation. *Nano Res.* **15**, 9985–10005 (2022).

54. Zhou Y. et al. Leaf-structure-inspired through-hole electrode with boosted mass transfer and photothermal effect for oxygen evolution reactions. *Adv. Functional Mater.* **33**, (2023).

55. Cao, Y. et al. Polar bear hair inspired supra-photothermal promoted water splitting. *ACS Mater. Lett.* **4**, 1912–1920 (2022).

56. Zheng, Q. et al. Reagent-adaptive active site switching on the IrO$_x$/Ni(OH)$_2$ catalyst. *Energy Environ. Sci.* **17**, 748–759 (2024).

57. Zhang Y. et al. Hetero-interface manipulation in MoO$_x$@Ru to evoke industrial hydrogen production performance with current density of 4000 mA cm^{-2}. *Adv. Energy Mater.* **13**, (2023).

58. Kozuch, S. et al. "Turning over" definitions in catalytic cycles. *ACS Catal.* **2**, 2787–2794 (2012).

59. Wu, L. et al. Boosting oxygen evolution reaction of (Fe,Ni)OOH via defect engineering for anion exchange membrane water electrolysis dnder industrial conditions. *Adv. Mater.* **35**, e2306097 (2023).

60. Sun H. et al. Electrochemical water splitting: bridging the gaps between fundamental research and industrial applications. *Energy. Environ. Mater.* **6**, (2023).

61. Yang H. et al. Self-supported electrocatalysts for practical water electrolysis. *Adv. Energy Mater.* **11**, (2021).

62. Li, H. et al. Systematic design of superaerophobic nanotube-array electrode comprised of transition-metal sulfides for overall water splitting. *Nat. Commun.* **9**, 2452 (2018).

63. Fernandez, D. et al. Bubble formation at a gas-evolving microelectrode. *Langmuir* **30**, 13065–13074 (2014).

64. Dastafkan, K. et al. Efficient oxygen evolution and gas bubble release achieved by a low gas bubble adhesive iron-nickel vanadate electrocatalyst. *Small* **16**, e2002412 (2020).

65. Liu, X. et al. Reconstruction-aetermined alkaline water electrolysis at industrial temperatures. *Adv. Mater.* **32**, e2001136 (2020).

66. Liu, X. et al. Complete reconstruction of hydrate pre-catalysts for ultrastable water electrolysis in industrial-concentration alkali media. *Cell. Rep. Phys. Sci.* **1**, 100241 (2020).

67. Zhang, B. et al. Simultaneous interfacial chemistry and inner Helmholtz plane regulation for superior alkaline hydrogen evolution. *Energy Environ. Sci.* **13**, 3007–3013 (2020).

68. Lu, Z. et al. Three-dimensional NiFe layered double hydroxide film for high-efficiency oxygen evolution reaction. *Chem. Commun.* **50**, 6479–6482 (2014).

69. Jiang, J. et al. Atomic-level insight into super-efficient electrocatalytic oxygen evolution on iron and vanadium co-doped nickel (oxy)hydroxide. *Nat. Commun.* **9**, 2885 (2018).

70. Su, W. et al. NiCo-LDH nanowires@nanosheets core-shell structure grown on carbon fiber cloth for high performance flexible supercapacitor electrode. *J. Alloy. Compd.* **799**, 15–25 (2019).

71. Wu, L. et al. Facile synthesis of nanoparticle-stacked tungsten-doped nickel iron layered double hydroxide nanosheets for boosting oxygen evolution reaction. *J. Mater. Chem. A* **8**, 8096–8103 (2020).

72. Liang, H. et al. Plasma-assisted synthesis of NiCoP for efficient overall water splitting. *Nano Lett.* **16**, 7718–7725 (2016).

73. Wu, Y. et al. Electron density modulation of NiCo$_2$S$_4$ nanowires by nitrogen incorporation for highly efficient hydrogen evolution catalysis. *Nat. Commun.* **9**, 1425 (2018).

74. Henkelman, G. et al. A climbing image nudged elastic band method for finding saddle points and minimum energy paths. *J. Chem. Phys.* **113**, 9901–9904 (2000).

75. Henkelman, G. et al. Improved tangent estimate in the nudged elastic band method for finding minimum energy paths and saddle points. *J. Chem. Phys.* **113**, 9978–9985 (2000).

Acknowledgements

Author contributions

Competing interests

The authors declare no competing interests.

Additional information

Supplementary information The online version contains supplementary material available at https://doi.org/10.1038/s41467-025-58320-5.

Correspondence and requests for materials should be addressed to Zhifeng Ren or Ghim Wei Ho.

Peer review information *Nature Communications* thanks Zhuofeng Hu, Shichun Mu and the other anonymous reviewer(s) for their contribution to the peer review of this work. A peer review file is available.

Reprints and permissions information is available at http://www.nature.com/reprints

Publisher's note Springer Nature remains neutral with regard to jurisdictional claims in published maps and institutional affiliations.